A Theoretical Formulation of Dilation/Contraction for Continuum Modelling of Granular Flows

Huabin Shi[1]†, Ping Dong[2], Xiping Yu[3] and Yan Zhou[2]

[1]State Key Laboratory of Internet of Things for Smart City and Department of Civil and Environmental Engineering, University of Macau, Avenida da Universidade, Taipa, Macao, China.

[2]School of Engineering, University of Liverpool, Brownlow Hill, Liverpool L69 3GH, United Kingdom.

[3]State Key Laboratory of Hydroscience and Engineering, Department of Hydraulic Engineering, Tsinghua University, Qinghuayuan, Beijing 100084, China.

(Received xx; revised xx; accepted xx)

Shear dilation/contraction of granular materials has long been recognized as an important process in granular flows but a comprehensive theoretical description of this process for a wide range of shear rate is not yet available. In this paper, a theoretical formulation of dilation/contraction is proposed for continuum modelling of granular flows in which the dilation/contraction effects consist of a frictional component resulting from the rearrangement of enduring-contact force chains among particles and a collisional component due to inter-grain collisions. In this formulation, a frictional solid pressure considering the rearrangement of contact force chains under shear deformation is proposed for the frictional dilation/contraction, while well-established rheological laws are adopted for the collisional inter-grain pressure to account for the collisional dilatancy effect. The proposed formulation is first verified analytically by describing the shear-weakening behaviour of granular samples in a torsional shear rheometer and by capturing the incipient failure of both dry and immersed granular slopes. It is then further validated numerically by integrating the proposed dilation/contraction formulation into a two-fluid continuum model and applying the model to study the collapse of submerged granular columns, in which the dilation/contraction plays a critical role.

Key words: …..

† Email address for correspondence: HuabinShi@um.edu.mo

1. Introduction

Dilation/contraction is an intrinsic property of granular materials when subjected to shear deformation and an important determinant of the behaviours of granular flows (Reynolds 1885; Wood 1990; Houssais & Jerolmack 2017). It strongly affects the onset of avalanches (Gravish & Goldman 2014), the initiation of submarine landslides (Rondon, Pouliquen & Aussillous 2011), and the liquefaction in debris flows (Kaitna, Dietrich & Hsu 2014). In submerged granular media, dilation/contraction would induce corresponding decrease/increase in the interstitial fluid pressure and relative motion between pore fluid and grains, which has a feedback on the granular skeleton and hence on the behaviours of granular flows (Meruane, Tamburrino & Roche 2010; Bouchut *et al.* 2016).

It is crucial to account for dilatancy effects in numerical models for granular flows (Bouchut *et al.* 2016). Although the dilation/contraction of granular materials has attracted intense interest in the past decades (Wood 1990; Pailha, Nicolas & Pouliquen 2008; Dsouza & Nott 2020), a quantitative description of the underlying dynamics and a generally accepted theoretical formulation of the dilatancy effects are still unavailable. Specifically, in continuum models for granular flows most of the existing formulations of dilation/contraction were empirical (Pailha & Pouliquen 2009; Iverson & George 2014; Delannay *et al.* 2017). For example, based on the critical state theory for quasi-static dry granular media in simple shear tests, Pailha & Pouliquen (2009) attributed the change in the volume of granular flows only to the quasi-static shear dilation/contraction and formulated it as the product of shear rate and the tangent of dilation angle in the continuity equation of granular flows. However, in the continuum theory, the volumetric change of granular flows equals to the divergence of flow velocity and is a combined result of various forces and processes such as advection, inter-grain collision and quasi-static dilation/contraction. The critical state theory of soil mechanics empirically accounts for only the part of volumetric change in granular flows due to the quasi-static dilation/contraction. Therefore, it is incomprehensive to attribute the total volumetric change of granular flows only to the quasi-static dilation/contraction and formulate it in the continuity equation based on the critical state theory as done in Pailha &

Pouliquen (2009). Similarly, the incomprehensiveness also exists in the formulation of Iverson & George (2014) even though they added one more contribution of effective inter-grain contact normal stress to the volumetric change. Unlike the above models that involve the dilation/contraction in the continuity equation, Guo *et al.* (2016) and Baumgarten & Kamrin (2019) considered the dilatancy effects in the momentum equation by integrating them into the plastic constitutive laws of granular materials. This type of models is consistent with the continuum theory and relates the dilation/contraction directly to inter-grain stresses.

Understanding the dynamics of dilation/contraction, i.e. what leads to this resultant behaviour of granular materials, helps to develop a theoretical formulation of the dilatancy effects. The widely-used critical state theory proposed by Roux and Radjai (1998) for quasi-static granular materials is an efficient empirical relation for the behaviour but cannot explain the reasons. For quasi-static granular media, Guo *et al.* (2016) and Baumgarten & Kamrin (2019) assumed that the dilation/contraction was due to the variation of inter-grain plastic stresses and formulated it by introducing a plastic shear deformation related to dilatancy in the constitutive laws of granular materials. At the other end, for rapid granular flows, the inter-grain collision force is taken to be the reason of dilatancy for which the kinetic theory (Jenkins & Savage 1983; Gonzalez-Ondina, Fraccarollo & Liu 2018) and rheological laws (Jop, Forterre & Pouliquen 2006) have been developed. However, these shear-rate-dependent theories for rapid flows cannot account for the contraction of granular materials and neither can they describe the dilation of quasi-static granular assemblies in which grains move rather slowly. A combination of the proposed dynamics for quasi-static granular media and rapid particulate flows may be applied to granular materials moving at a wide range of shear rate.

In this paper, a theoretical description of dilation/contraction is presented for continuum modelling of granular flows based on the spatially-filtered and Favre-averaged continuity and momentum equations. It is proposed that the dilation/contraction effects in sheared granular flows consist of a frictional portion resulting from the rearrangement of enduring-contact force chains among the particles and a collisional portion due to inter-grain collision force, which are respectively accounted for by the frictional and the collisional solid pressure in the

continuum model. A new formulation of the frictional solid pressure considering the rearrangement of contact force chains under shear deformation is proposed while the collisional solid pressure is estimated by well-established rheological laws. The proposed formulation is analytically validated both in describing the shear-weakening behaviour of dry granular samples in a torsional shear rheometer and in predicting the incipient failure of dry and immersed granular slopes. The frictional and the collisional dilation/contraction effects are integrated into the two-fluid Smoothed Particle Hydrodynamics (SPH) model for granular flows developed in Shi *et al.* (2019). The model is then used to further verify the proposed theoretical formulation of dilation/contraction by simulating submerged granular column collapse, a benchmark in which the dilation/contraction plays a critical role from the initiation of the collapse to the final deposition. The dramatic influences of initial packing fraction on the collapsing column profile and the evolution of interstitial fluid pressure due to dilation/contraction of granular materials are all well reproduced.

The rest of the paper is structured as follows. A continuum description of granular flows is briefly given in section 2. The proposed formulation of dilation/contraction is introduced in section 3. Analytical validations are presented in section 4 and numerical verifications in simulations of underwater granular column collapse are conducted in section 5. Finally, conclusions are given in section 6.

2. A continuum description of granular flows

The spatially-filtered and Favre-averaged continuity and momentum equations in Shi *et al.* (2019) are adopted here for a continuum description of granular flows. They are

$$\frac{\partial\left(\phi_s\rho_s\right)}{\partial t}+\nabla\cdot\left(\phi_s\rho_s\boldsymbol{u}_s\right)=0 \tag{2.1}$$

$$\frac{\partial\left(\phi_s\rho_s\boldsymbol{u}_s\right)}{\partial t}+\nabla\cdot\left(\phi_s\rho_s\boldsymbol{u}_s\boldsymbol{u}_s\right)=\nabla\cdot\left(\phi_s\boldsymbol{\sigma}_s\right)+\phi_s\rho_s\boldsymbol{g}+\nabla\cdot\left(\phi_s\boldsymbol{\sigma}_s^t\right)-\phi_s\nabla p_f+\boldsymbol{F}\,, \tag{2.2}$$

in which the subscript s represents the solid phase and f indicates the interstitial fluid in granular media; t is the time; ϕ_s is the solid volume fraction; ρ_s is the particle material

density; $\boldsymbol{u}_s$ is the velocity; $\boldsymbol{\sigma}_s$ is the inter-grain stress tensor of the solid phase excluding the pressurization of the grains due to the interstitial fluid pressure; $\boldsymbol{g}$ is gravitational acceleration; $\boldsymbol{\sigma}_s^t$ is a stress tensor of the solid phase due to interstitial fluid turbulence; p_f is the interstitial fluid pressure; $\boldsymbol{F}$ denotes the inter-phase forces other than the buoyancy. $\boldsymbol{F}$ generally consists of drag force, lift force, and virtual-mass force but can be simplified as drag force when the dense granular flows are studied in which drag force is predominant (Baumgarten & Kamrin 2019). In subaerial granular media, the solid stress $\boldsymbol{\sigma}_s^t$, the interstitial air pressure p_f, and the drag force $\boldsymbol{F}$ by air on the particles are neglected. In immersed granular materials, p_f is resolved, $\boldsymbol{\sigma}_s^t$ is determined by introducing a turbulence model, and $\boldsymbol{F}$ is estimated by the formula proposed by Gidaspow (1994), as shown in section 5.1.

$\boldsymbol{\sigma}_s$ consists of stresses resulting from inter-grain collisions and enduring contacts. It is expressed as

$$\boldsymbol{\sigma}_s = 2\rho_s \nu_s \boldsymbol{S}_s - p_s \boldsymbol{I}, \tag{2.3}$$

where

$$\boldsymbol{S}_s = \frac{1}{2}\left[\nabla \boldsymbol{u}_s + \left(\nabla \boldsymbol{u}_s\right)^{\mathrm{T}}\right] - \frac{1}{3}\left(\nabla \cdot \boldsymbol{u}_s\right)\boldsymbol{I}; \tag{2.4}$$

$\boldsymbol{I}$ is the identity matrix; ν_s and p_s are respectively the solid viscosity and pressure due to inter-grain collisions and enduring contacts.

A frictional constitutive law that is widely used in granular flows and intense sediment transport (Maurin, Chauchat & Frey 2016; Heyman *et al.* 2017) is adopted to determine the viscosity ν_s of the granular materials. ν_s is related to the inter-grain pressure p_s as

$$\nu_s = \frac{\mu p_s}{2\rho_s \left\|\boldsymbol{S}_s\right\|}, \tag{2.5}$$

where μ is the friction coefficient and is estimated by the rheological law in section 3.3; the second invariant $\left\|\boldsymbol{S}_s\right\| = \sqrt{\boldsymbol{S}_s : \boldsymbol{S}_s / 2}$. The inter-grain solid pressure p_s consists of two components (Johnson & Jackson 1987):

$$p_s = p_s^e + p_s^c, \tag{2.6}$$

where p_s^e is caused by enduring contacts among the granular particles and p_s^c is due to the collisions between the grains. The frictional component p_s^e accounts for the solid-like

behaviour of dense gently-flowing granular materials (Johnson, Nott & Jackson 1990). It generally increases with the volume fraction of the granular assembly ϕ_s and vanishes when ϕ_s is below the random loose-packing fraction ϕ_*. In almost all of the existing formulas for p_s^e, the pressure only varies with ϕ_s and is independent of shear rate (van Wachem *et al.* 2001). A new formulation of p_s^e taking the dilation/contraction effects and the influence of shear rate into account is proposed in section 3.2. The shear-rate-dependent collisional component p_s^c is a dominant contribution to p_s in rapid granular flows and responsible for the increase in the volume of rapidly flowing granular materials (Forterre & Pouliquen 2008). The formulation of p_s^c will be detailed in section 3.3.

3. Shear dilation/contraction

3.1. A new dilation/contraction framework

To describe the dilation/contraction process of both quasi-static and rapid flowing granular materials, a new dilation/contraction framework is proposed. It suggests that the dilatancy effects in sheared granular flows consist of a frictional portion resulting from the rearrangement of enduring-contact force chains among the particles and a collisional portion due to inter-grain collisions, corresponding to the two components of solid pressure. The collisional dilatancy effect has been well studied (Forterre & Pouliquen 2008) while a formulation of the frictional dilation/contraction remains unavailable and is the focus of this paper.

Figure 1 sketches the frictional dilation/contraction. It is postulated that the frictional dilation and contraction of granular materials arise respectively from the sharp increase and decrease of the frictional solid pressure p_s^e as a result of the rearrangement of contact force chains among the particles. As shown in figure 1(a), when the initially densely packed granular medium is sheared to a strain of γ, there is an intensification of the microscopic contact force chains leading to an increase in the macroscopic solid pressure p_s^e. The increased inter-grain pressure pushes the particles up, leading to an expansion of the granular

medium and an increase in the porosity. In immersed granular media, the enlargement of void volume between grains results in a decrease of pore pressure. Conversely, in figure 1(b), the contact force chains in the loosely packed granular assembly break down resulting in the decrease of frictional solid pressure and contraction of the particle assembly as well as a decrease in the porosity. In immersed granular media, the shrinkage of inter-grain void volume leads to an increase in the pore pressure. A formulation of the changes in p_s^e due to the rearrangement of contact force chains is proposed in section 3.2.

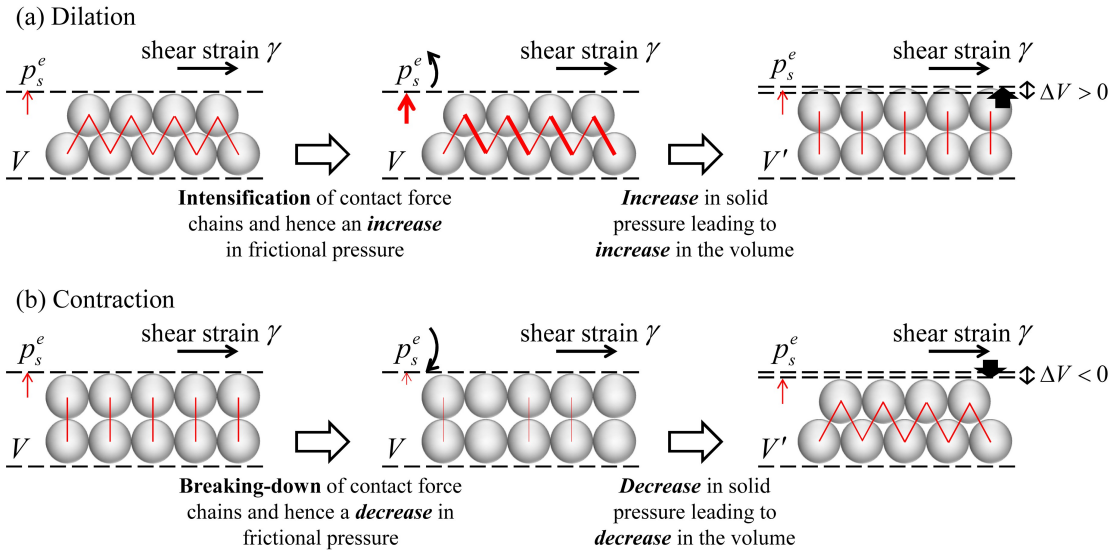

Figure 1. Sketches of the frictional dilation/contraction. The red solid lines linking the grains roughly represent the enduring-contact force chains among granular particles, and the red upward arrows below the symbol p_s^e represent the macroscopic frictional solid pressure. The thickness of the red lines roughly indicates the magnitude of contact forces and the length of the red arrows denotes that of p_s^e.

3.2. Frictional dilation/contraction

To quantify the frictional dilation/contraction effect in granular flows, here a formulation of the changes in p_s^e due to the rearrangement of contact force chains is proposed. We consider a granular assembly with a packing fraction of ϕ_s sheared at a finite rate. According to the introduced framework in figure 1, the change in the packing fraction due to frictional

dilation/contraction against an increment of shear strain $\partial\gamma$ results from the variation of p_s^e, expressed as

$$\frac{\partial \phi_s}{\partial \gamma} = -\left|\frac{\partial \phi_s}{\partial p_s^e}\right| \frac{\partial p_s^e}{\partial \gamma}. \tag{3.1}$$

The negative sign in (3.1) indicates that an increase or decrease of p_s^e respectively leads to a decrease or increase in ϕ_s, as illustrated in figure 1. A similar expression was adopted by Lu, Brodsky & Kavehpour (2007) to describe the shear-weakening behaviour of granular materials. Through multiplying (3.1) by $-\left|\partial p_s^e / \partial \phi_s\right|$, the changes in p_s^e when $p_s^e > 0$ and $\phi_s > 0$ can be estimated by

$$\frac{\partial p_s^e}{\partial \gamma} = -\left|\frac{\phi_s}{p_s^e}\frac{\partial p_s^e}{\partial \phi_s}\right| \frac{p_s^e}{\phi_s}\frac{\partial \phi_s}{\partial \gamma}. \tag{3.2}$$

As in Rowe (1962), a dilatancy angle ψ is defined as:

$$\tan\psi = \frac{1}{V}\frac{\partial V}{\partial \gamma} = -\frac{1}{\phi_s}\frac{\partial \phi_s}{\partial \gamma}, \tag{3.3}$$

where V is the volume of the granular assembly and ∂V is the volumetric change due to frictional dilation/contraction. (3.3) implies that the mass of the granular assembly keeps constant during frictional dilation/contraction. By defining $\Re \equiv \left|\left(\phi_s / p_s^e\right)\partial p_s^e / \partial \phi_s\right|$ and combining (3.2) and (3.3), we have

$$\frac{\partial p_s^e}{\partial \gamma} = \Re p_s^e \tan\psi. \tag{3.4}$$

Note that (3.4) is applicable for any time instant. As the rearrangement of contact force chains takes place at the particle scale, the corresponding changes in the pressure occur in a very short duration of $O\left(d_s / \sqrt{p_s^e / \rho_s}\right)$ (see Forterre & Pouliquen 2008, d_s is the particle diameter), during which there is an exceedingly small shear strain increment of γ_* in the granular assembly. In this strain change, we replace the p_s^e in the definition of $\Re$ by p_{s0}^e as a first approximation and obtain

$$\Re \approx \left|\frac{\phi_s}{p_{s0}^e}\frac{\partial p_{s0}^e}{\partial \phi_s}\right|, \tag{3.5}$$

in which p_{s0}^e is the frictional solid pressure excluding the frictional dilation/contraction

effect and is a function of ϕ_s. Hence, both $\Re$ and $\tan\psi$ are macroscopic properties of the granular assembly varying with the volume fraction ϕ_s on a timescale of $O\left(1/2\|\boldsymbol{S}_s\|\right)$. In granular media whose behaviours are dominated by inter-grain frictional contacts, the ratio of the timescale for the microscopic contact-force chain rearrangement to that for changes in macroscopic properties, i.e. $O\left(2d_s\|\boldsymbol{S}_s\|/\sqrt{p_s^e/\rho_s}\right)$, has a value of $O\left(10^{-6}\right)\sim O\left(10^{-1}\right)$ (Lu, Brodsky & Kavehpour 2007; Chialvo, Sun & Sundaresan 2012). Therefore, it is reasonable to regard the microscopic rearrangement of contact-force chains and adjustment of the solid pressure as a transient process in a continuum description of granular flows and during this period the macroscopic properties of the granular assembly $\Re$ and $\tan\psi$ stay unchanged. We can then rearrange (3.4) to $\partial p_s^e/p_s^e=\left(\Re\tan\psi\right)\partial\gamma$ and integrate it over $\left[0,\gamma_*\right]$, which gives

$$p_s^e = p_{s0}^e e^{\Re\gamma_*\tan\psi}. \tag{3.6}$$

In general, the frictional solid pressure excluding the dilation/contraction effect p_{s0}^e is a function of the solid volume fraction and can be computed by a few existing formulas (Johnson & Jackson 1987; van Wachem *et al.* 2001; Hsu, Jenkins & Liu 2004). Without loss of generality, p_{s0}^e can be determined by

$$p_{s0}^e=\begin{cases} G\left(\phi_s-\phi_*\right)^{\chi} & \phi_s>\phi_* \\ 0 & \phi_s\le\phi_* \end{cases}, \tag{3.7}$$

where ϕ_* is the random loose-packing volume fraction; G is a compressibility coefficient of the grains, which is related to the Young's modulus and the Poisson's ratio of the solid material; χ is a parameter to characterize the arrangement of contact force chains, which generally varies from 1.50 to 5.50 (Hsu, Jenkins & Liu 2004; Lee & Huang 2018). Rewriting (3.6) in terms of the packing fraction ($0<\phi_s-\phi_*<1$) as

$$p_s^e = p_{s0}^e\left(\phi_s-\phi_*\right)^{\frac{\Re\gamma_*\tan\psi}{\ln\left(\phi_s-\phi_*\right)}}, \tag{3.8}$$

and combining (3.7) and (3.8), we obtain

$$p_s^e = G\left(\phi_s-\phi_*\right)^{\chi+\Delta\chi} = G\left(\phi_s-\phi_*\right)^{\chi+\frac{\Re\gamma_*\tan\psi}{\ln\left(\phi_s-\phi_*\right)}} \tag{3.9}$$

for $\phi_s>\phi_*$. (3.9) indicates that the change of p_s^e results from the adjustment of the parameter χ for the arrangement of contact force chains, consistent with the proposed

framework in figure 1.

By applying (3.7) to obtain $\partial p_{s0}^e / \partial \phi_s$ and p_{s0}^e in (3.5) for the case of $\phi_s > \phi_*$, we have

$$\Re \approx \frac{\chi \phi_s}{\phi_s - \phi_*}. \tag{3.10}$$

Regarding to the dilatancy angle, the critical state theory in Roux & Radjai (1998) is employed, i.e.

$$\tan\psi = K\left(\phi_s - \phi_c\right), \tag{3.11}$$

in which K is a material parameter of granular assembly varying in the range of 1.0 ~ 25.0 and can be determined through simple shear tests (Pailha & Pouliquen 2009; Bonnet, Richard & Philippe 2010; Gravish & Goldman 2014); ϕ_c is the critical volume fraction of dilatancy, at which there is no frictional dilation/contraction effect. ϕ_c may vary with the imposed force and the shear rate (Bouchut *et al.* 2016) and in this paper is related to the flow dimensionless number I_m following Iverson & George (2014), written as

$$\phi_c = \frac{\phi_{c0}}{1+\sqrt{I_m}}, \tag{3.12}$$

where the dimensionless number I_m is a combination of the inertia number and the viscous number of granular flows, defined by (3.18); ϕ_{c0} is the critical volume fraction of dilatancy for static granular materials when $I_m = 0$.

The shear strain γ_* increases with the temporal duration of the microscopic rearrangement of inter-grain contact force chains, the scale of which is $d_s / \sqrt{p_{s0}^e / \rho_s}$ (for simplification, here we use p_{s0}^e rather than p_s^e), and with the rate of the macroscopic mean deformation of the granular assembly, $2\|\boldsymbol{S}_s\|$. A non-dimensional shear rate I_d can thus be defined as

$$I_d \equiv \frac{2 d_s \|\boldsymbol{S}_s\|}{\sqrt{p_{s0}^e / \rho_s}}, \tag{3.13}$$

and γ_* increases with I_d. It is noted that I_d is utilized to quantify the shear strain of granular media in the process of frictional dilation/contraction and is different from the inertia number $I_i \equiv 2 d_s \|\boldsymbol{S}_s\| / \sqrt{p_s / \rho_s}$. A preliminary analysis on the magnitude of γ_* in appendix A suggests that γ_* has a small order of $O\left(10^{-2}\right) \sim O\left(10^{-1}\right)$ and

$$\gamma_* = c_1 I_d^{c_2}, \tag{3.14}$$

where c_1 and c_2 are coefficients. The analysis gives $c_1 = 0 \sim O(10)$ and $c_2 = 0 \sim 1$.

Combining (3.6), (3.10), and (3.11), we have the frictional solid pressure including the frictional dilation/contraction effect expressed as

$$p_s^e = p_{s0}^e \exp\left[K \frac{\chi \phi_s}{\phi_s - \phi_*} (\phi_s - \phi_c) \gamma_* \right]. \tag{3.15}$$

In (3.15), the frictional solid pressure is related to the shear strain γ_*. Further, combining (3.15) and (3.14), we can relate the frictional solid pressure to the shear rate of granular flows as

$$p_s^e = p_{s0}^e \exp\left[c_1 K \frac{\chi \phi_s}{\phi_s - \phi_*} (\phi_s - \phi_c) I_d^{c_2} \right]. \tag{3.16}$$

(3.16) is valid when $\phi_s > \phi_*$ and $p_s^e = p_{s0}^e = 0$ when $\phi_s \le \phi_*$.

3.3. Collisional dilatancy

The rheological law proposed in Trulsson, Andreotti & Claudin (2012) is adopted for the collisional dilatancy effect. The shear-rate-dependent collisional solid pressure p_s^c is determined by

$$p_s^c = 2 \left(\frac{c_3 \phi_s}{\phi_0 - \phi_s} \right)^2 \left(\rho_f \nu_f + 2 c_4 \rho_s d_s^2 \|\boldsymbol{S}_s\| \right) \|\boldsymbol{S}_s\|, \tag{3.17}$$

in which ϕ_0 is the jamming volume fraction, the maximum packing fraction of sheared granular materials in a steady state; ρ_f is the density of interstitial fluid and ν_f is its kinematic viscosity; d_s is the diameter of granular particles; c_3 and c_4 are coefficients. In general, $c_3 = 0.75 \sim 3.00$ and $c_4 = 0 \sim 1.00$ (Chauchat 2018; Lee & Huang 2018). The effect of interstitial fluid viscosity is included in (3.17) but can be neglected when considering subaerial granular flows.

The rheological law relates the friction coefficient μ in (2.5) to a dimensionless number I_m of granular flows, which is a combination of the inertia number I_i and the viscous number $I_\nu \equiv 2\|\boldsymbol{S}_s\| \rho_f \nu_f / p_s$. It is defined as

$$I_m \equiv I_v + c_4 I_i^2 = \frac{2\|\boldsymbol{S}_s\|\left(\rho_f \nu_f + 2c_4 \rho_s d_s^2 \|\boldsymbol{S}_s\|\right)}{p_s}, \tag{3.18}$$

in which c_4 is the same coefficient with that in (3.17). A small value of I_m indicates that the granular flow moves at a low speed and is in the quasi-static regime, while a large value of I_m corresponds to a rapid granular flow in the inertia regime (Forterre & Pouliquen 2008). According to Trulsson, Andreotti & Claudin (2012), the friction coefficient depends on I_m as

$$\mu = \mu_1 + \frac{\mu_2 - \mu_1}{1 + \sqrt{I_0 / I_m}}, \tag{3.19}$$

where $\mu_1 = \tan\varphi$ is the friction coefficient when $I_m = 0$ and the granular assembly is in static; φ is the internal friction angle of the grains; $\mu_2 = \tan\varphi \sim 1.0$ is the friction coefficient when I_m is infinite and the granular assembly flows fairly rapidly; I_0 is a model parameter and is set to be a value close to the characteristic I_m of the flow (Boyer, Guazzelli & Pouliquen 2011).

4. Analytical verifications of the dilation/contraction formulation

4.1. Shear-Weakening behaviour of granular samples

The experimental data of sheared granular samples within a torsional shear cell in Lu, Brodsky & Kavehpour (2007) is used to verify the proposed theoretical formulation of dilation/contraction. In the experiment, a granular sample composed of sifted beach sand, having a mean diameter of $d_s = 438\,\mu\text{m}$, a density of $\rho_s = 2.65\,\text{g}/\text{cm}^3$, and an internal frictional angle of $\varphi = 37.5^\circ$, was sheared in a top-rotating torsional shear rheometer. The rheometer was a highly sensitive feedback controlled instrument with the normal force, top-plate height and angular velocity monitored simultaneously, which hence can directly provide the values of inter-grain pressure, packing fraction and shear rate in the granular sample for the theory validation. The granular sample was initially loaded up to a height of 6 mm with a packing fraction of $\phi_s = 0.61$ when static. It was then sheared by rotating the top plate at a finite angular velocity with the column height staying fixed and the volume fraction

of the medium keeping constant. The normal stress on the top plate was recorded. The shear angular velocity ω varied from 0.001 rad/s to 100 rad/s in different experimental cases and the shear rate of the granular sample was correspondingly between 0.001 s^{-1} and 2800 s^{-1}. It was shown in the results that the normal stress on the top plate varied little when the angular shearing velocity ω was lower than 0.01 rad/s but became negatively correlated with ω when ω was increased up to 25 rad/s, demonstrating a shear-weakening rheology with a dip of the normal stress. As ω increased further, the normal stress increased almost quadratically with the shear rate when the grains came to be in the inertia regime.

At the steady state when the sample is sheared at a rate of $\dot{\gamma}$, the normal stress on the top plate σ is balanced by the inter-grain pressure p_s as

$$\sigma = p_s = p_s^e + p_s^c . \tag{4.1}$$

Excluding the effect of interstitial fluid viscosity in (3.17) for subaerial granular samples and combining (3.12), (3.16), (3.17) and (4.1), the normal stress varies with the shear rate $\dot{\gamma} = 2\|\boldsymbol{S}_s\|$ as

$$\sigma = p_{s0}^e \exp\left[c_1 K \frac{\chi\phi_s}{\phi_s - \phi_*}\left(\phi_s - \phi_c\right) I_d^{c_2} \right] + c_4 \left(\frac{c_3\phi_s}{\phi_0 - \phi_s} \right)^2 \rho_s d_s^2 \dot{\gamma}^2 . \tag{4.2}$$

The frictional solid pressure without the dilation/contraction effect p_{s0}^e, determined by (3.7), balances the initially imposed normal stress σ_0 to the static granular sample at the start of each experimental case, i.e.

$$\sigma_0 = p_{s0}^e = G\left(\phi_s - \phi_*\right)^{\chi} . \tag{4.3}$$

Dividing both sides of (4.2) by σ_0, we have the dimensionless normal stress varying with shear rate as

$$\frac{\sigma}{\sigma_0} = \exp\left[c_1 K \frac{\chi\phi_s}{\phi_s - \phi_*}\left(\phi_s - \phi_c\right) I_d^{c_2} \right] + c_4 \left(\frac{c_3\phi_s}{\phi_0 - \phi_s} \right)^2 \frac{\rho_s d_s^2 \dot{\gamma}^2}{\sigma_0} , \tag{4.4}$$

in which the non-dimensional shear rate $I_d = d_s\dot{\gamma}\big/\sqrt{\sigma_0/\rho_s}$. Figure 2 shows the comparisons between the results of (4.4) and the measured data. In the experiment, $\sigma_0 = 1.25\times10^4$ Pa, $\phi_* = 0.590$, and a random close-packing fraction $\phi^* = 0.640$. A jamming volume fraction $\phi_0 = 0.630$ is set which is in a reasonable range of $\phi_s \sim \phi^*$. The compressibility coefficient

of the natural sand G is 10^9 Pa , and according to (4.3) the coefficient $\chi = \ln(\sigma_0/G)/\ln(\phi_s - \phi_*)$ is 2.89. A critical volume fraction of dilatancy $\phi_{c0} = 0.630$ is estimated in the experiment. The parameter K was not measured and we take $c_1 K$ as a single coefficient. $c_1 K = 1.50$ and $c_2 = 0.42$ are set by fitting the computed results with the data in both quasi-static and transitional regimes, while $c_3 = 1.80$ and $c_4 = 0.0005$ are determined according to the fitness in the inertia regime. Values of the parameters are summarized in table 1.

As shown in figure 2 the predicted variation of the normal stress against shear rate agrees well with the measured data, which demonstrates that the proposed formulation of frictional solid pressure is capable of describing the shear-weakening behaviour of the granular sample. It shows that when the sample is in the quasi-static and the transitional regimes the frictional solid pressure p_s^e predominates and the decrease in p_s^e due to the frictional contraction is the reason for the dip in the normal stress. When the sample is in the inertia regime, the collisional inter-grain pressure p_s^c increases quadratically with the shear rate and becomes dominant in the balance with the normal stress on the top-plate. (4.4), which is a direct result of the proposed dilation/contraction theory, can map the variation of the normal stress imposed to the sheared sample smoothly between the quasi-static and the inertia regimes.

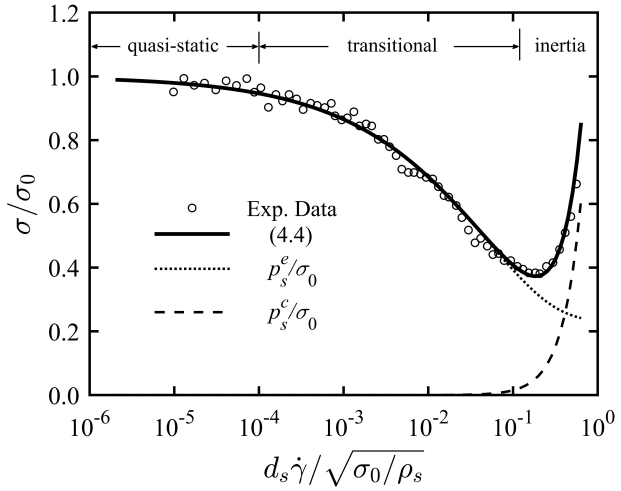

Figure 2. Variation of normal stress on the rheometer top-plate with non-dimensional shear rate in the volume-constant experiments of Lu, Brodsky & Kavehpour (2007). The non-dimensional frictional solid pressure p_s^e/σ_0 and collisional pressure p_s^c/σ_0 are computed by the first and the second terms on the right-hand side of (4.4), respectively.

4.2. Incipient failure of granular slopes

In this section, the proposed theoretical formulation is assessed through predicting the incipient failure of dry and immersed granular slopes.

Gravish and Goldman (2014) experimentally studied the effects of initial packing fraction on the failure of dry granular slopes. An initially horizontal layer of grains with $d_s = 256\,\mu\text{m}$, $\rho_s = 2.5\,\text{g}/\text{cm}^3$ and volume fraction ϕ_s ranging between 0.58 and 0.63 was prepared on a fluidized bed. The bed was then rotated to a 45° angle with a constant rate. The granular motion in the bed was recorded by cameras, and the instant when incipient motion of grains on the surface occurred was detected. The angle of the slope at the instant θ_0, referred to as incipient angle, was then obtained according to the rotation rate of the bed. In different experimental cases, the initial packing fraction was varied and different failure behaviors of the granular slopes were observed. It was found that the bed with a packing fraction smaller than the critical value $\phi_{c0} = 0.595 \pm 0.003$ experienced a rapid failure and a compaction, while the bed with a fraction larger than the critical value underwent a slow failure and a dilation. Specifically, the bed with initial $\phi_s = 0.58$ had an incipient angle of $\theta_0 = 7.7 \pm 1.4^\circ$, whereas the θ_0 of the bed with $\phi_s = 0.63$ was $32.1 \pm 1.5^\circ$. Overall, the incipient angle of the slopes increased significantly with the initial packing fraction.

First, for comparison, the classical saw model of dilatancy (Rowe 1962; Pailha & Pouliquen 2009) is applied to estimate the incipient angle of granular slopes. In the theory, forces are in equilibrium both along and normal to the slope and the dilation/contraction affects the slope failure by leading to a change in the angle of shearing. At the critical incipient state, the grains on the bed surface are controlled by

$$\phi_s p_s \tan\delta = \phi_s \rho_s g h \sin\theta_0 \tag{4.5}$$

$$\phi_s p_s = \phi_s \rho_s g h \cos\theta_0 \tag{4.6}$$

$$\text{and} \quad \tan\delta = \tan\left(\varphi + \psi\right), \tag{4.7}$$

where δ is the angle of shearing; φ is the internal friction angle of the grains and $\tan\varphi$ is the friction coefficient when there is no dilatancy effect; h is a characteristic depth of the

grains to move. Recall that ψ is the dilatancy angle. (4.5) and (4.6) are respectively for the balance of forces in the directions along and normal to the slope. Combining (4.5) – (4.7) as well as (3.11), we have

$$\theta_0 = \varphi + \psi = \varphi + \arctan\left[K\left(\phi_s - \phi_c\right)\right]. \tag{4.8}$$

$\phi_c = \phi_{c0}$ holds during the incipient failure of the slopes.

Here, we apply the proposed formulation to predict the incipient angle of granular slopes. It should be noted that the collisional solid pressure p_s^c vanishes at the incipient failure stage and thus $p_s = p_s^e$. When the granular bed is static, in the direction normal to the slope, the inter-particle pressure without the frictional dilation/contraction effect p_{s0}^e balances the gravity as

$$\phi_s p_s = \phi_s \rho_s g h \cos\theta_0, \tag{4.9}$$

$$\text{where} \quad p_s = p_{s0}^e = G\left(\phi_s - \phi_*\right)^\chi. \tag{4.10}$$

Hence, $p_{s0}^e = G\left(\phi_s - \phi_*\right)^\chi = \rho_s g h \cos\theta_0$. As it approaches to the critical incipient state, before the incipient motion is detected, the grains on the slope surface undergo a small shear strain γ_* during the failure. Due to the rearrangement of contact force chains along with the strain, the solid pressure changes from $p_s = p_{s0}^e$ to $p_s = p_{s0}^e e^{\Re\gamma_* \tan\psi}$ in the frictional dilation/contraction and the forces in the direction normal to the slope cease to be in equilibrium. In the densely-packed granular slope, the solid pressure increases and the resultant force in the normal direction becomes upward, leading to a dilation of the assembly. Conversely, in the loosely-packed granular bed, the solid pressure decreases and the resultant force directs downward, inducing a contraction in the bed. In the direction along the slope, the equilibrium condition is still valid. Hence,

$$\phi_s p_s \tan\varphi = \phi_s \rho_s g h \sin\theta_0, \tag{4.11}$$

$$\text{where} \quad p_s = p_{s0}^e e^{\Re\gamma_* \tan\psi} = \rho_s g h \cos\theta_0 e^{\Re\gamma_* \tan\psi}. \tag{4.12}$$

Effect of the dilation/contraction on the friction coefficient during the incipient period is neglected. Combining (4.11) and (4.12) gives

$$\tan\theta_0 = e^{\Re\gamma_* \tan\psi} \tan\varphi, \tag{4.13}$$

407 which can be written explicitly as

408 $$\theta_0 = \varphi + \arctan\left[\frac{e^{\Re\gamma_* \tan\psi} - 1}{1/\tan\varphi + e^{\Re\gamma_* \tan\psi}\tan\varphi}\right]. \tag{4.14}$$

409 Substituting $\chi\phi_s/(\phi_s - \phi_*)$ for $\Re$ and $K(\phi_s - \phi_c)$ for $\tan\psi$ as in section 3, we finally
410 obtain

411 $$\theta_0 = \varphi + \arctan\left[\frac{e^{c\phi_s(\phi_s-\phi_c)/(\phi_s-\phi_*)} - 1}{1/\tan\varphi + e^{c\phi_s(\phi_s-\phi_c)/(\phi_s-\phi_*)}\tan\varphi}\right], \tag{4.15}$$

412 where $c = \chi\gamma_* K$. It is noted that in this case we do not apply (3.14) to replace γ_* with $c_1 I_d^{c_2}$
413 but keep γ_* in the equation as a parameter because the shear rate of the slope during the
414 incipient motion is not measureable. Moreover, it is more reasonable to relate the incipient
415 dynamics of granular slopes at critical state to the shear strain than to the shear rate. In
416 Gravish & Goldman (2014), the measured critical volume fraction of dilatancy ϕ_c was 0.595,
417 the material parameter for dilatancy K was 22.4, and the internal friction angle of grains in
418 the air φ was 17.0°. A random loose-packing volume fraction of $\phi_* = 0.570$ is determined
419 according to the experimental setup. χ=3.50 is set which is the median value of its range
420 (see section 3.2 and table 1). A shear strain of $\gamma_* = 0.026$, consistent with the analysis in
421 appendix A, is obtained by fitting the results with the experimental data.

422 Figure 3 compares the computed incipient angles of the granular slope using (4.8) and
423 (4.15) with the measured data. It can be seen that the results given by the present formulation
424 agree with the data much better than those by the classical saw model, especially when the
425 initial packing fraction of the granular slope is larger than the critical value of dilatancy and
426 the bed dilates.

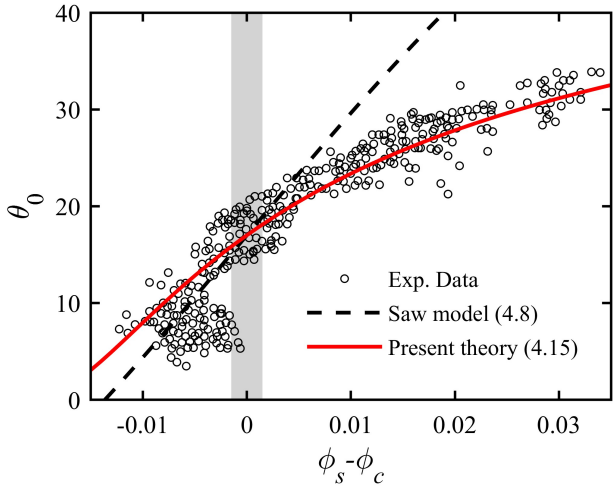

Figure 3. Variation of the incipient angle of dry granular slope with the initial packing fraction in the experiment of Gravish & Goldman (2014). The measured critical volume fraction $\phi_c = 0.595$ with the grey bar indicating the measurement uncertainty.

Bonnet, Richard & Philippe (2010) conducted a similar experiment to study the failure of immersed granular slopes in static water ($\rho_f = 1.0\,\mathrm{g/cm^3}$). The grains had a diameter of $d_s = 600\,\mu\mathrm{m}$ and a density of $\rho_s = 2.65\,\mathrm{g/cm^3}$. The initial packing fraction of the granular particles in the bed ϕ_s varied from 0.52 to 0.59 and the corresponding measured incipient angle of the slopes varied significantly, having a notably high ratio of 2.5 between the maximal and the minimal values. It should be noted that the shear strain and the deformation of the free granular slope during the incipient stage are expected to be exceedingly small and accordingly the variation of pore pressure is not appreciable and neglected here. Therefore, the buoyancy of the grains is accounted for by substituting $\rho_s - \rho_f$ for ρ_s in (4.5) – (4.6) and (4.9) – (4.12). Consequently, both (4.8) of the saw model and (4.15) of the present frictional dilation/contraction theory can also be applied to determine the incipient angle of immersed granular slopes.

Figure 4 shows the comparisons between the computed results and the measured data. According to the experimental results in Bonnet, Richard & Philippe (2010), the parameter $K = 20.8$, the critical volume fraction of dilatancy $\phi_c = 0.545$, and the internal friction angle of gains in the water $\varphi = 38.6^\circ$. A random loose-packing volume fraction of $\phi_* = 0.510$ is roughly determined as the minimal value of the packing fraction prepared in the experiment

was between 0.51 and 0.52. Same as that in the dry slope case, a value of $\chi = 3.50$ is also set. According to the verification against measured data, a shear strain of $\gamma_* = 0.019$ is adopted, which has the same order as that in the dry slope case. Values of parameters are summarized in table 1. It is shown in figure 4 that the computed incipient angle by the present formulation agrees generally well with the measured data and the fitness is better than that between the results of the classical saw model and the data. The present formulation performs well in the dilation situation and only slightly overestimates the incipient angle when the bed experiences a contraction. For the cases of $\phi_s - \phi_c \le -0.02$ where the incipient angle seems to vary little with the packing fraction, both the present theory and the classical saw model have an underestimation, which may be due to the lack of fluid viscosity's effect on slope failures. In immersed granular media, solid particles have an additional cohesion due to the viscosity of interstitial fluid, noted as c'. At the critical state, along the slope there is a balance between the additional particle cohesion, the inter-particle shear stress, and the gravity as $\phi_s \left(c' + p_s \tan\varphi \right) = \phi_s \left(\rho_s - \rho_f \right) gh \sin\theta_0$. In the cases of $\phi_s - \phi_c \le -0.02$, due to frictional contraction, the inter-particle pressure and shear stress decrease significantly and could have a smaller value than c'. As a result, the additional particle cohesion predominates in resisting the incipient motion of the slope, yielding $\theta_0 = \arcsin\left[c' / \left(\rho_s - \rho_f \right) gh \right]$. Assuming a same value of c' for the cases with different packing fractions, we can find that the slope incipient angle varies little with the packing fraction. For an accurate quantification of the phenomenon, more measured data are required in further investigations.

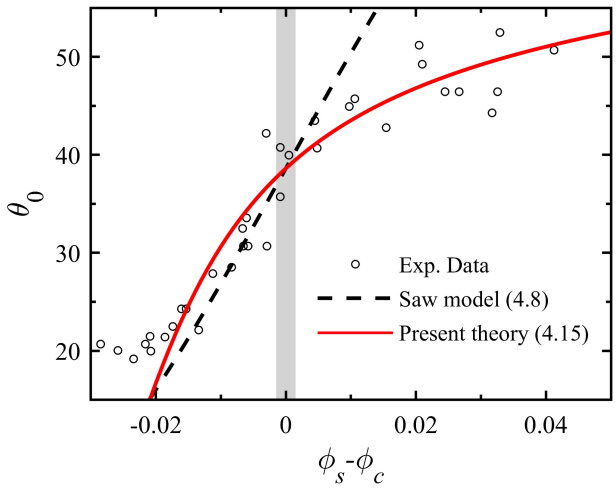

Figure 4. Variation of the incipient angle of immersed granular slopes in water with the initial packing fraction in the experiment of Bonnet, Richard & Philippe (2010). The measured critical volume fraction is $\phi_c = 0.545$ and the grey bar represents the uncertainty in the measurement.

5. Numerical validations by simulations of submerged granular column collapse

The proposed dilation/contraction formulation is integrated into the two-fluid model of Shi *et al.* (2019) which is validated in laminar bed-load transport by Poiseuille flow (see appendix B) and in this section is applied to simulate submerged granular column collapse. The submerged granular mass collapse is a benchmark for studying the dilation/contraction of granular materials, in which the frictional dilation/contraction plays a critical role in the whole process from the initiation of the crash to the final deposition (Houssais & Jerolmack 2017; Baumgarten & Kamrin 2019). It has been shown in the experiments that the initially loosely-packed columns exhibited a fast initiation of motion and compacted in the collapse with an increase in the pore fluid pressure while the densely-packed columns collapsed rather slowly and dilated with a decrease in the pore fluid pressure (Rondon, Pouliquen & Aussillous 2011; Wang *et al.* 2017). A two-phase model fully resolving the primary variables of the solid and the liquid phases helps to capture the dynamics in the dilation/contraction of the saturated granular materials.

5.1. A two-phase continuum model based on Smoothed Particle Hydrodynamics method

The present dilation/contraction theory is integrated into the model of Shi et al. (2019), which is a two-phase continuum model based on the weakly compressible Smoothed Particle Hydrodynamics (WCSPH) method. The controlling equations, i.e. conservation equations of mass and momentum of the two phases, are obtained by first averaging the physical variables of each phase in a control volume following Drew (1983) for a continuum description of both phases and then spatially filtering via Favre averaging for turbulence. The equations are then written into Lagrangian form for numerical implementation using SPH method. Here, for brevity, we only give a minimum description of the model. Detailed derivation of the equations and numerical implementations of the model can be found in Shi, Yu & Dalrymple (2017) and Shi *et al.* (2019).

The governing equations of the solid phase are,

$$\frac{d\phi_s}{dt} = -\phi_s \nabla \cdot \boldsymbol{u}_f - \nabla \cdot \left[\phi_s \left(\boldsymbol{u}_s - \boldsymbol{u}_f \right) \right], \tag{5.1}$$

$$\frac{d\boldsymbol{u}_s}{dt} = -\left[\left(\boldsymbol{u}_s - \boldsymbol{u}_f \right) \cdot \nabla \right] \boldsymbol{u}_s + \frac{1}{\phi_s \rho_s} \nabla \cdot \left(\phi_s \boldsymbol{\sigma}_s \right) + \boldsymbol{g} + \frac{1}{\phi_s \rho_s} \nabla \cdot \left(\phi_s \boldsymbol{\sigma}_s^t \right) - \frac{1}{\rho_s} \nabla p_f + \frac{\boldsymbol{F}}{\phi_s \rho_s}, \tag{5.2}$$

and those of the interstitial fluid phase are,

$$\frac{d\left(\phi_f \rho_f \right)}{dt} = -\left(\phi_f \rho_f \right) \nabla \cdot \boldsymbol{u}_f, \tag{5.3}$$

$$\frac{d\boldsymbol{u}_f}{dt} = \frac{1}{\phi_f \rho_f} \nabla \cdot \left(\phi_f \boldsymbol{\tau}_f \right) + \boldsymbol{g} + \frac{1}{\phi_f \rho_f} \nabla \cdot \left(\phi_f \boldsymbol{\tau}_f^t \right) - \frac{1}{\rho_f} \nabla p_f - \frac{\boldsymbol{F}}{\phi_f \rho_f}. \tag{5.4}$$

In the equations, ρ_f, $\boldsymbol{u}_f$, and ϕ_f are respectively the density, velocity, and volumetric fraction of the fluid phase; $\boldsymbol{\tau}_f$ and $\boldsymbol{\tau}_f^t$ are the kinetic and the turbulent shear stresses of the fluid phase, respectively. Other notations have the same meaning as in section 2. For any physical variable X, $d\mathrm{X}/dt = \partial \mathrm{X}/\partial t + \left(\boldsymbol{u}_f \cdot \nabla \right) \mathrm{X}$. It indicates that the velocity of a SPH particle is set to be the same with the fluid velocity it carries. When concerning saturated granular flows, we have $\phi_s + \phi_f = 1$.

The constitutive law integrating the present dilation/contraction formulation is utilized to determine the inter-grain stress of the solid phase as

$$\boldsymbol{\sigma}_s = 2\rho_s \nu_s \boldsymbol{S}_s - p_s \boldsymbol{I} = 2\rho_s \nu_s \boldsymbol{S}_s$$

512
$$-\left\{ p_{s0}^e \exp\left[c_1 K \frac{\chi \phi_s}{\phi_s - \phi_*} \left(\phi_s - \phi_c\right) I_d^{c_2} \right] + 2\left(\frac{c_3 \phi_s}{\phi_0 - \phi_s} \right)^2 \left(\rho_f \nu_f + 2 c_4 \rho_s d_s^2 \left\| \boldsymbol{S}_s \right\| \right) \left\| \boldsymbol{S}_s \right\| \right\} \boldsymbol{I}, \tag{5.5}$$

513
$$\nu_s = \frac{\mu p_s}{2\rho_s \left\| \boldsymbol{S}_s \right\|}, \tag{5.6}$$

514
$$\text{and} \quad \mu = \mu_1 + \frac{\mu_2 - \mu_1}{1 + \sqrt{I_0 / I_m}}. \tag{5.7}$$

515 The combined dimensionless number for immersed granular flows, I_m, is calculated by
516 (3.18), which is recalled here as

517
$$I_m = \frac{2\left\| \boldsymbol{S}_s \right\| \left(\rho_f \nu_f + 2 c_4 \rho_s d_s^2 \left\| \boldsymbol{S}_s \right\| \right)}{p_s}. \tag{5.8}$$

518 $\boldsymbol{S}_s$ is defined as (2.4) and $\left\| \boldsymbol{S}_s \right\| = \sqrt{\boldsymbol{S}_s : \boldsymbol{S}_s / 2}$. The notations have the same meaning as in
519 sections 2 and 3. The frictional solid pressure without dilation/contraction effect p_{s0}^e can be
520 determined by (3.7), which is a general form of existing formulas for p_{s0}^e. However, for
521 comparison with the model of Shi *et al.* (2019) excluding the frictional dilation/contraction
522 effect, the formula of p_{s0}^e adopted in Shi *et al.* (2019) is also used in this section. It is shown
523 as

524
$$p_{s0}^e = \begin{cases} G\left(\phi_s - \phi_*\right)^\chi \left[1 + \sin\left(\dfrac{\phi_s - \phi_*}{\phi^* - \phi_*} \pi - \dfrac{\pi}{2} \right) \right] & \phi_s > \phi_* \\ 0 & \phi_s \le \phi_* \end{cases}, \tag{5.9}$$

525 where ϕ^* is the random close-packing volume fraction of the granular assembly. The
526 difference between (5.9) and (3.7) is simply the inclusion of volume fraction ϕ_s for the
527 compressibility of grains. It only leads to a minor difference in the values of χ and has no
528 notable effect on the results.

529 The stress of the solid phase induced by interstitial fluid turbulence $\boldsymbol{\sigma}_s^t$ is usually
530 neglected in subaerial granular flows. In submerged cases, it is expressed as

531
$$\boldsymbol{\sigma}_s^t = 2\rho_s \nu_s^t \boldsymbol{S}_s - p_s^t \boldsymbol{I}, \tag{5.10}$$

532 in which ν_s^t and p_s^t are respectively the turbulent viscosity and pressure of the solid phase
533 indicating the effects of interstitial fluid turbulence on grains. In dense granular flows, p_s^t is

534 generally much smaller than p_s and can therefore be neglected (Bouchut *et al.* 2016;
535 Baumgarten & Kamrin 2019). ν_s^t is estimated by a Smagorinsky turbulence model in (5.13).
536 The kinetic and the turbulent shear stresses of the fluid phase are formulated as

537 $$\boldsymbol{\tau}_f = 2\rho_f \nu_f \boldsymbol{\mathcal{S}}_f, \tag{5.11}$$

538 $$\text{and } \boldsymbol{\tau}_f^t = 2\rho_f \nu_f^t \boldsymbol{\mathcal{S}}_f, \tag{5.12}$$

539 where ν_f is the fluid kinematic viscosity and ν_f^t is the turbulent viscosity of the fluid
540 phase. ν_f^t, together with the turbulent solid viscosity ν_s^t, is estimated by the Smagorinsky
541 model proposed in Dalrymple & Rogers (2006) but integrated with a modification for the
542 turbulence damping by solid particles. It is shown as

543 $$\nu_k^t = 2\left(C_{S,k}\Delta\right)^2 \left\|S_k\right\| \left(1-\frac{\phi_s}{\phi^*}\right)^n, \tag{5.13}$$

544 in which the subscript $k = f, s$; Δ is the size of SPH particles; $C_{S,k}$ is the Smagorinsky
545 coefficient and in this paper we set $C_{S,f} = C_{S,s} = 0.1$; the index n is for the effects of
546 turbulence damping by solid particles and $n = 5$ is adopted according to Chen *et al.* (2011)
547 and Shi *et al.* (2019).
548 In submerged dense granular flows, the inter-phase force $\boldsymbol{F}$ can be simplified to
549 include only the drag force that is predominant. The formula proposed by Gidaspow (1994) is
550 adopted to estimate the drag force as

551 $$\boldsymbol{F} = \phi_s \beta \left(\boldsymbol{u}_f - \boldsymbol{u}_s\right), \tag{5.14}$$

552 $$\text{where } \beta = \begin{cases} \dfrac{3}{4} C_D \dfrac{\rho_f \left|\boldsymbol{u}_f - \boldsymbol{u}_s\right|}{d_s} \phi_f^{-1.65} & \phi_s \le 0.2 \\ 150 \dfrac{\phi_s \rho_f \nu_f}{\phi_f d_s^2} + 1.75 \dfrac{\rho_f \left|\boldsymbol{u}_f - \boldsymbol{u}_s\right|}{d_s} & \phi_s > 0.2 \end{cases} \tag{5.15}$$

553 $$\text{and } C_D = \begin{cases} \dfrac{24}{Re_s}\left(1.0 + 0.15 Re_s^{0.687}\right) & Re_s < 1000 \\ 0.44 & Re_s \ge 1000 \end{cases}. \tag{5.16}$$

554 C_D is the drag coefficient and Re_s is the particle Reynolds number, defined by
555 $Re_s \equiv \phi_f \left|\boldsymbol{u}_f - \boldsymbol{u}_s\right| d_s / \nu_f$. $\left|\boldsymbol{u}_f - \boldsymbol{u}_s\right|$ is the norm of the relative velocity between the two

556 phases.

557 In the WCSPH method, the fluid is assumed to be weakly compressible and thus ρ_f is
558 not a constant. Hence, one more equation is required to close the model. The equation of state
559 proposed by Shi, Yu & Dalrymple (2017) is used to relate the fluid pressure p_f in the
560 solid-liquid mixture to the variable fluid density, shown as

561 $$p_f = \frac{\rho_{f0} c_0^2}{\xi} \frac{\phi_f \rho_f + \phi_s \rho_{f0}}{\phi_f \rho_f} \left[\left(\frac{\phi_f \rho_f + \phi_s \rho_{f0}}{\rho_{f0}} \right)^{\xi} - 1 \right], \tag{5.17}$$

562 where ρ_{f0} is the reference density of the fluid when $p_f = 0$; ξ is a material parameter;
563 c_0 is the sound speed in the fluid at the reference density. Usually, for numerical stability, a
564 value of ten times the maximum flow velocity in the problem is adopted. In the present
565 simulations of submerged granular column collapse, $\xi = 7$ and $c_0 = 25\,\mathrm{m/s}$ are set for the
566 viscous liquid used in the experiments.

567 *5.2. Model parameter characterizing the frictional dilation/contraction*

568 Rondon, Pouliquen & Aussillous (2011) had conducted a well-known experiment of
569 submerged granular column collapse in a viscous fluid using an experimental set-up as
570 illustrated in figure 5. The experimental flume was 70 cm-long, 15 cm-wide, 15 cm-high and
571 filled with liquid having a density of $\rho_f = 1.0\,\mathrm{g/cm^3}$ and a kinematic viscosity of
572 $\nu_f = 1.2 \times 10^{-5}\,\mathrm{m^2/s}$ to a depth of $H = 15\,\mathrm{cm}$. Initially, the granular column was confined by
573 a removable gate at the left end of the flume. The column was composed of glass beads of
574 density $\rho_s = 2.5\,\mathrm{g/cm^3}$, mean diameter $d_s = 225\,\mu\mathrm{m}$, and internal friction angle $\varphi = 20.0^\circ$.
575 The horizontal and the vertical directions are respectively defined as x and z. The columns
576 were well prepared to a finite packing fraction, being in either loose-packing or dense-packing
577 states. In the cases studied in this paper, the columns had a fixed width of 6 cm in x
578 direction, and the initial depth of the columns h varied. In the loose-packing case,
579 $h = 4.8\,\mathrm{cm}$ and the initial mean volume fraction of the column was $\overline{\phi}_s = 0.55$. In the
580 dense-packing case, $h = 4.2\,\mathrm{cm}$ and $\overline{\phi}_s = 0.60$. A slight variation of volume fraction over the
581 depth due to the gravity existed in the columns but only the depth-averaged value was

measured. A critical volume fraction of dilatancy $\phi_{c0} = 0.58$ was observed in the measured data, around which there was a transition in the behaviours between the loosely- and the densely-packed columns (Rondon, Pouliquen & Aussillous 2011). Once the gate was suddenly removed (in less than 0.1 s), the column collapsed.

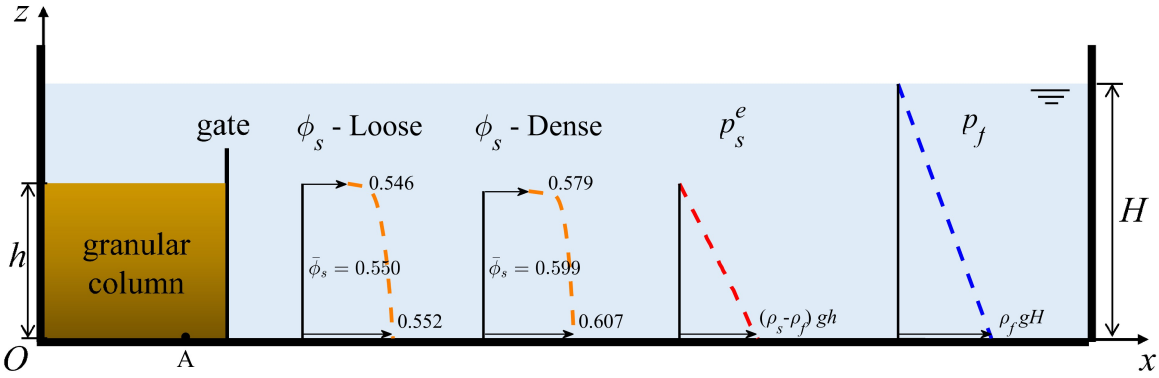

Figure 5. A schematized representation of the experimental set-up by Rondon, Pouliquen & Aussillous (2011), also showing the profiles of the initial solid volume fraction in the loosely- and densely-packed columns, the linear profile of inter-grain pressure $p_s = p_s^e = p_{s0}^e$ in the initially static columns, and the hydrostatic profile of fluid pressure p_f.

To simulate a problem such as submerged granular column collapse, especially its time evolution process, it is essential to determine the initial conditions of all necessary variables as closely as possible. As the initial inter-grain pressure in the static columns $p_s = p_s^e = p_{s0}^e$ is to resist the immersed weight of grains, initial values of p_{s0}^e must satisfy the static condition and have an almost linear distribution over the depth. Once the collapse starts, the frictional inter-grain pressure may increase or decrease due to the rearrangement of contact force chains, leading to the frictional dilation or contraction of the granular assembly and distinct collapsing behaviours. However, in previous work on this problem (Lee & Huang 2018; Si, Shi & Yu 2018), the static condition for initial inter-grain pressure was not met and the model parameters in the formulas of p_{s0}^e were determined through only matching computed and measured collapsing behaviours of the columns. The change in frictional inter-grain pressure due to rearrangement of contact force chains that leads to the dilation/contraction of the granular assembly was not considered in previous models. As a result, in their models, the initial values of inter-grain pressure in the stationary

605 loosely-packed column were smaller while those in the stationary densely-packed column
606 were much greater than the static immersed weight of the grains. Indeed, the initial inter-grain
607 pressure to balance the immersed weight of the static loosely-packed and densely-packed
608 columns is close as the original heights of the two columns are similar with $h = 4.8\,\text{cm}$ in
609 the loose packing case and $h = 4.2\,\text{cm}$ in the dense packing case. The reason for the similar
610 initial inter-grain pressure in the two columns with essentially different porosities is the
611 difference in the arrangement of contact-force chains among solid grains. Therefore, the
612 parameter χ in the formula of p_{s0}^{e} that characterizes the effect of contact-force chains
613 arrangement on the frictional solid pressure has different values in the two cases. Once the
614 column collapses, χ adjusts according to the proposed $\Delta\chi$ in (3.9), leading to a change in
615 the frictional solid pressure and the frictional dilation/contraction of granular columns.

616 The parameters $\phi_* = 0.540$ and $\phi^* = 0.625$ are chosen so that all the values of the
617 prepared packing fraction in the experiment are in the range of $\phi_* \sim \phi^*$. The compressibility
618 coefficient G for glass beads is 10^9 Pa. To achieve a linear profile of initial inter-grain
619 pressure in the static columns, i.e. $p_s(z)\big|_{t=0} = p_{s0}^{e}(z) = (\rho_s - \rho_f) g (h - z)$, the initial volume
620 fraction is set to slightly vary vertically but have a same mean value with the experimental
621 setup. The value of χ is determined carefully so that the initial ϕ_s varies in a narrow range.
622 For the loose packing case, χ is set to be $\chi = 2.64$ and the initial volume fraction
623 increases from $\phi_s = 0.546$ on the surface to $\phi_s = 0.552$ at the bottom with a vertical average
624 value of $\overline{\phi}_s = 0.550$. For the dense packing case, $\chi = 5.50$ is set and the initial ϕ_s
625 increases from $\phi_s = 0.579$ downwards to $\phi_s = 0.607$ with an average value of $\overline{\phi}_s = 0.599$.
626 The profiles of the initial volume fraction and the initial solid pressure are shown in figure 5.

627 The coefficients in (5.5) for the frictional solid pressure are set to be $c_1 K = 2.5$ and
628 $c_2 = 0.10$ according to the model calibrations. The parameter K of the used granular
629 material was not measured in the experiment and in the simulations $c_1 K$ is taken as a single
630 parameter. The other coefficients in the model are determined following a sensitivity study in
631 appendix C as: $c_3 = 2.50$, $c_4 = 0.10$, and $\phi_0 = 0.610$ for the collisional solid pressure in
632 (5.5); $\mu_2 = 0.8$ and $\sqrt{I_0} = 0.005$ for the friction coefficient in (5.7). Values of all the
633 material and the adjustable parameters are summarized in table 1.

634 The proposed model is numerically implemented on the basis of the open-source weakly
635 compressible SPH-package GPUSPH (Hérault, Bilotta & Dalrymple 2010). The
636 computational domain is represented by 111 192 SPH particles which have an initial size of
637 $\Delta = 0.002\,\mathrm{m}$. The fixed time step of the simulations is $\Delta t = 10^{-5}\,\mathrm{s}$. The parallel computations
638 are conducted on an Nvidia Tesla K40c CUDA-enabled Graphics Processing Units (GPU)
639 card, which has 2880 processor cores and a compute capability of 3.5. It takes about 4.2 h of
640 computational time to simulate 4 s of the column collapse.

641 *5.3. Column profiles and pore-pressure feedback*

642 Figures 6 and 7 show the comparisons between the computed column profiles and the
643 measured data in the loose-packing and the dense-packing cases, respectively. Results
644 computed by the present model that includes both the frictional and the collisional
645 dilation/contraction effects and by the model of Shi *et al.* (2019) which does not account for
646 the frictional dilation/contraction effect are presented together for comparison. The
647 coefficients in the two models are the same. It can be seen that in both cases there is a general
648 agreement between the column profiles computed by the present model with the experimental
649 data, especially a good agreement in the final depositions. For the loose packing case, once
650 the gate is removed, the whole upper part of the column crashes down immediately. The flow
651 front moves rapidly and then stops in 4 s at $x = 22.1\,\mathrm{cm}$ resulting in a long runout distance.
652 The final deposition of the column is triangular. For the dense packing case, only grains at the
653 right edge of the column fall freely after the gate is removed, while most of the column keeps
654 static. The collapse goes inward with time and the flow front moves forward smoothly. The
655 flow front stops at $x = 12.0\,\mathrm{cm}$ and the collapse process ends in 33 s with a
656 trapezium-shaped final deposition. The present model clearly captures the distinct behaviours
657 of the initially loosely- and densely-packed columns, while the model of Shi *et al.* (2019)
658 without accounting for the frictional dilation/contraction effect fails. The model of Shi *et al.*
659 (2019) produces similar results for the two cases, in which the collapse of the loosely-packed
660 column is much slower while that of the densely-packed column is slightly quicker than the
661 corresponding results from the present model. The comparisons between the results of the two

662 models demonstrate the importance of the frictional dilation/contraction effect and the
663 predicative capability of the present model integrating the proposed dilation/contraction
664 formulation.

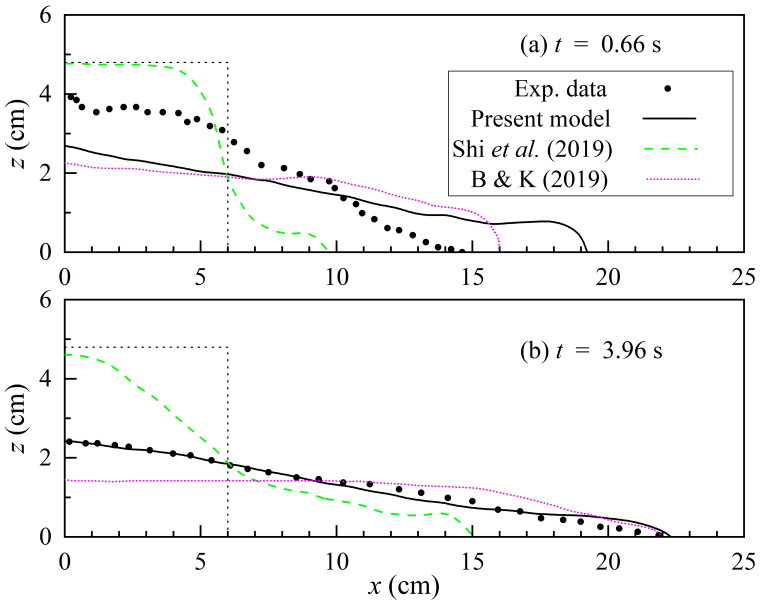

665

666 Figure 6. Comparisons between the computed and the measured column profiles in the loose packing
667 case. The black dotted lines represent the initial profile of the column. The present model considers the
668 frictional dilation/contraction effect while the model of Shi *et al.* (2019) does not. The magenta
669 short-dotted curves are the column profiles computed by the model of Baumgarten & Kamrin (2019),
670 abbreviated as "B & K (2019)" in the figure for brevity, which has also taken the dilation/contraction
671 into account.

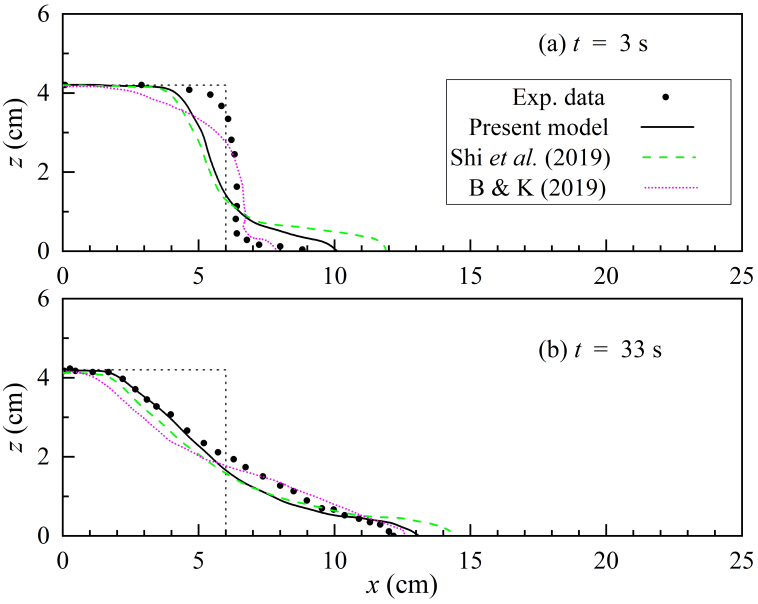

672

673 Figure 7. Same as figure 6 but for the results in the dense packing case.

674 Another notable phenomenon resulting from the dilation/contraction of submerged
675 granular collapse is the change of pore pressure in the column. Rondon, Pouliquen &
676 Aussillous (2011) reported that the pore pressure at the bottom of the granular column
677 increased while decreased quickly in the loose and the dense packing cases once the collapse
678 started, respectively. In the present two-phase model, the pore-pressure feedback in
679 dilation/contraction is implicitly taken into account by coupling the controlling equations of
680 the two phases through the drag force and the constant total volumetric fraction. In the
681 collapse of immersed granular columns, the rearrangement of contact-force chains induces a
682 variation of inter-grain frictional stress which further leads to an expansion/contraction of the
683 solid phase and hence a relative motion between the solid and the liquid phases. In the case of
684 dilation, the expansion of the solid phase results in an increase in the column porosity and the
685 liquid phase is pulled by the inter-phase drag force to expand, both of which induces a
686 decrease in the pore pressure. Conversely, in the case of contraction, the pore pressure
687 increases due to a decrease in the column porosity and a squeeze on the liquid phase by the
688 drag force. Figure 8 shows the computed excess fluid pressure in the experimental domain at
689 the early stage of the collapse. It can be clearly seen in figure 8(a) and 8(c) that the pore
690 pressure in the granular column computed by the present model increases in the loose packing

case while decreases in the dense packing case, consistent with the experimental observations. In figure 8(b) and 8(d), values of the excess pore pressure computed by the model without the frictional dilation/contraction effect are negative in both the loose and the dense packing cases, which differs markedly from the measurements. Hence, it is verified in figure 8 that the pore-pressure feedback can be reasonably captured by the present two-phase model integrating the proposed frictional dilation/contraction formulation.

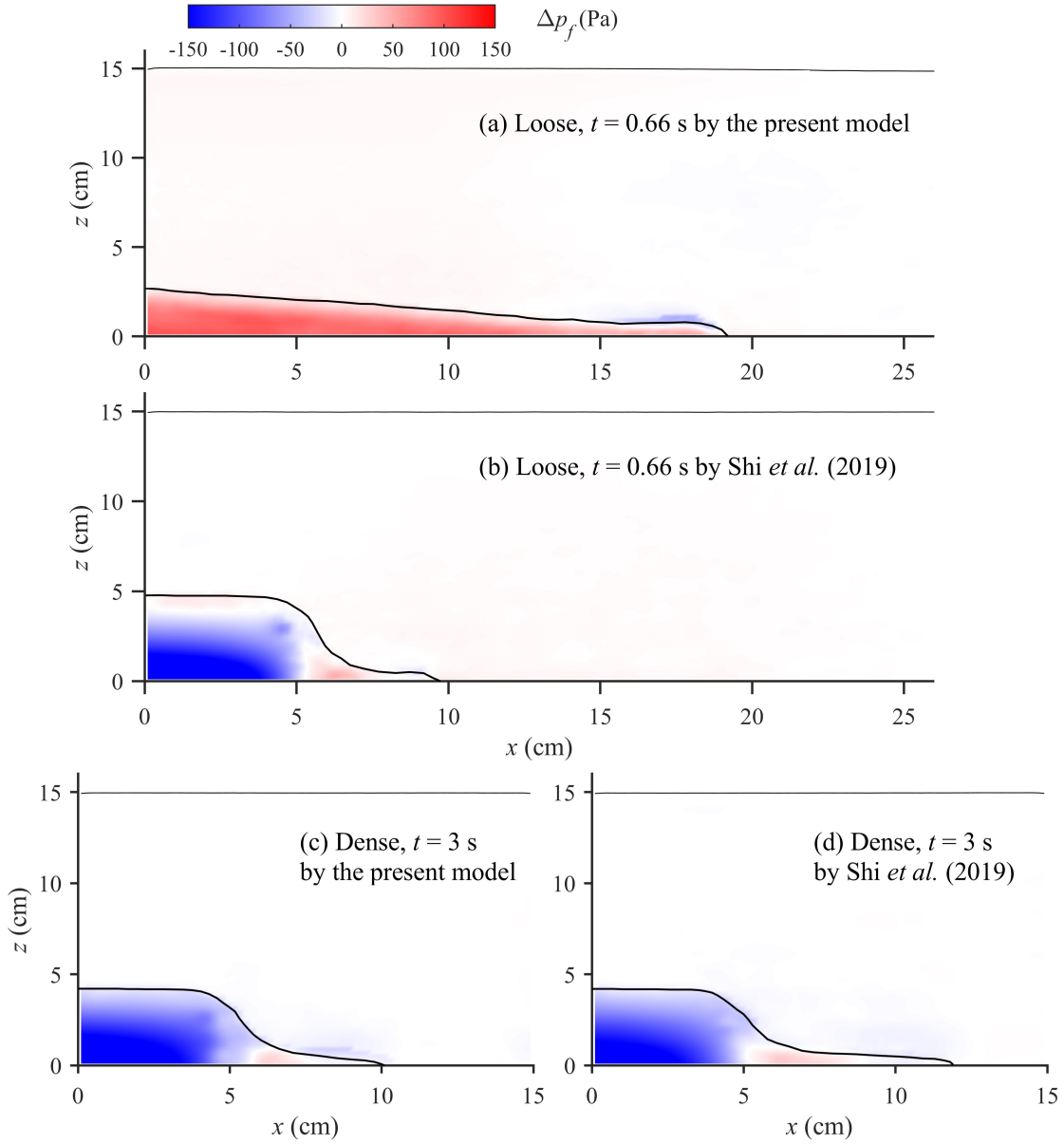

Figure 8. Computed excess fluid pressure by the present model (with the frictional dilation/contraction) and the model of Shi *et al.* (2019) (without the frictional dilation/contraction). The black solid curves in the liquid represent the computed column profiles.

The computed variations of excess pore pressure and solid volume fraction at Point A (shown in figure 5) by the present model are given in figure 9. In the loose packing case, the pore pressure increases rapidly once the column collapses and the maximum value of the computed excess pore pressure is about 210 Pa, slightly larger than available measured data. In the dense packing case, the pore pressure initially decreases significantly and then the excess pore pressure relaxes to zero. In both cases, the computed relaxation time by the present model is shorter than the experimental results, especially in the loose packing case. It should be noted that the fluctuations in the pressure are caused by the WCSPH numerical method itself. Figure 9 also shows that the solid volume fraction at Point A in the loose packing case increases slightly and the fraction in the dense packing case decreases, corresponding respectively to the contraction and the dilation of the columns.

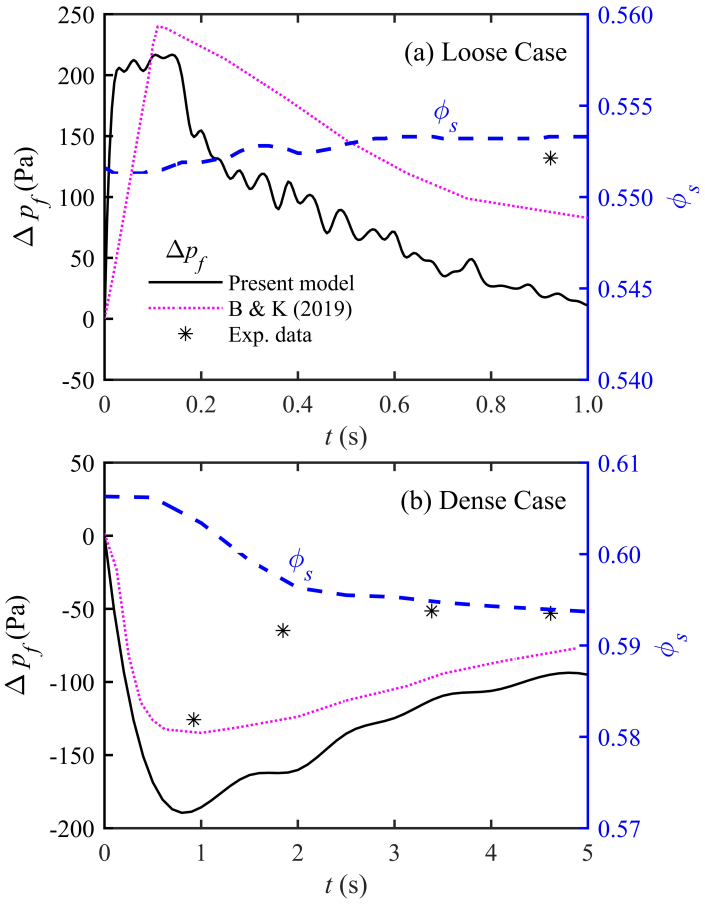

Figure 9. Variations of excess pore pressure and solid volume fraction at Point A. The position of Point A is shown in figure 5. The magenta dotted curves are for the results computed by the model of Baumgarten & Kamrin (2019), abbreviated as "B & K (2019)" in the figures for brevity.

For further investigations on the performance of the proposed dilation/contraction formulation, figures 6, 7, and 9 also compare the computed results by the present model with those by the model of Baumgarten & Kamrin (2019). In their plastic constitutive law of granular materials, Baumgarten & Kamrin (2019) integrated the dilatancy effect by adding a term of solid volumetric change to the plastic strain rate, which had a more complicate form than the present formulation. It is shown in figures 6 and 7 that in the early stage of collapse the computed column height by the present model agrees better with the measured data while the computed front position by Baumgarten & Kamrin (2019) fits the data better. In both figures, the final deposition of the columns computed by the present model compares much better with the experimental observations. Figure 9, together with figure 14(a) of Baumgarten & Kamrin (2019), shows that their model performs better in describing the variation of pore pressure even though there was a violent fluctuation in their results.

5.4. Discussions

The only difference between the two-phase model in this paper and that of Shi *et al.* (2019) is the integration of the frictional dilation/contraction effect on the inter-grain pressure. As stated in section 5.2, when simulating the column collapse, Shi *et al.* (2019) like other previous work on granular flow models (such as Lee & Huang 2018) neglected the initial condition for inter-grain pressure and calibrated the model parameters in the formula of p_{s0}^{e} according to the collapsing behaviours. When we set the parameters to make sure the initial values of p_{s0}^{e} satisfy the static condition to balance the immersed weight of grains as done in this paper, it is clearly shown that the model of Shi *et al.* (2019) without the frictional dilation/contraction effect fails to reproduce the distinct collapsing behaviours of initially loosely- and densely-packed columns while the present model succeeds. Therefore, integrating the proposed formulation of the frictional dilation/contraction effect helps us to capture the column collapse from the initially static state to the final deposition.

It should be noted that there is still room for improvement in the present two-phase model. Figures 6 and 7 show that in the early stage of the collapse the present model predicts a faster motion of flow front than the experimental observations. According to the sensitivity

744 study in appendix C, the reason for this faster collapse is probably the underestimation of the
745 collisional solid pressure p_s^c and the corresponding inter-grain shear resistance. Moreover,
746 the faster collapse in the early stage results in a rapid dissipation of excess pore pressure at the
747 bottom of the column and hence a smaller pore-pressure relaxation time than the observed.
748 Further improvement in the formulation of the collisional solid stresses is required.

749 The well-posedness of the present two-phase model is required to be further investigated,
750 even though the simulations in this paper are stable. It has been pointed out by Barker *et al.*
751 (2015; 2017) that the μ(I) rheological model is ill-posed when the inertial number I_i is too
752 high or too low and including compressibility, rate dependence, and viscous dissipation could
753 help to stabilize the computation. In the present model the effect of interstitial fluid viscosity
754 on granular rheology has been integrated and the liquid adopted in the presented experiments
755 of immersed granular column collapse had a high viscosity. It is most likely that the viscous
756 dissipation induced by interstitial liquid makes the present simulations stable.
757

Parameters	Varying Ranges	Is a Material Parameter?	Values			
			Section 4.1	Section 4.2 (Dry Cases)	Section 4.2 (Immersed Cases)	Section 5
ϕ_*	$0.500 \sim 0.600$	YES	0.590	0.570	0.510	0.540
ϕ^*	$0.580 \sim 0.640$	YES	0.640	0.640	0.620	0.625
G	$O(10^4) \sim O(10^9)$ (Pa)	YES	10^9	---	---	10^9
χ	$1.50 \sim 5.50$	NO	2.89	3.50	3.50	2.64 (loose) 5.50 (dense)
ϕ_{c0}	$\phi_* \sim \phi^*$	YES	0.630	0.595	0.545	0.580
K	$1.0 \sim 25.0$	YES	$c_1K = 1.5$	22.4	20.8	$c_1K = 2.5$
c_1	$0 \sim O(10)$	NO		---	---	
c_2	$0 \sim 1.00$	NO	0.42	---	---	0.10
$\gamma_* = c_1 I_d^{c_2}$	$O(10^{-2}) \sim O(10^{-1})$	NO	---	0.026	0.019	---
c_3	$0.75 \sim 3.00$	NO	1.80	---	---	2.50
c_4	$0 \sim 1.00$	NO	0.0005	---	---	0.10
ϕ_0	$\phi_* \sim \phi^*$	YES	0.630	---	---	0.610
μ_1	$\tan\varphi$	YES	$\tan(37.5^\circ)$	$\tan(17.0^\circ)$	$\tan(38.6^\circ)$	$\tan(20.0^\circ)$
μ_2	$\tan\varphi \sim 1.0$	NO	---	---	---	0.8
I_0	$0 \sim 1.0$	NO	---	---	---	2.5×10^{-5}

TABLE 1. Parameters in the model. The third column shows whether a parameter is a material parameter, whose value is determined depending on the physical properties of solid grains and according to related experimental observations. In sections 4.1 and 5, the material parameter K was not measured and we take c_1K as a single adjustable parameter. In section 4.2, when concerning the critical incipient state of granular slopes, the frictional solid pressure is related to the shear strain γ_* and $\gamma_* = c_1 I_d^{c_2}$ is taken as an adjustable parameter. In specific analytical cases, if its value is not set, the parameter is not involved in the solutions.

6. Conclusions

Shear dilation/contraction plays a significant role in geological granular flows from the initial destabilization to final deposition. Neither the critical state theories in soil mechanics nor the shear-rate-dependent rheological laws are generally applicable to fully describing the dilatancy effects in granular flows at a wide range of shear rate. This paper presents a theoretical description of dilation/contraction for continuum modelling of granular flows. It is based on the understanding that the dilatancy effects in sheared granular materials consist of a frictional portion resulting from the rearrangement of enduring-contact force chains and a collisional portion owing to inter-grain collisions. The frictional dilation/contraction can be accounted for by the changes in the frictional solid pressure for enduring contacts between grains while the collisional dilatancy is considered by the shear-rate-dependent collisional solid pressure in rheological laws for granular flows. A new analytical formulation of the frictional solid pressure considering the rearrangement of contact force chains under shear deformation is proposed for the first time in this paper.

The proposed dilation/contraction formulation accurately captures the shear-weakening behaviour of granular samples in a torsional shear rheometer and the incipient failure of dry and immersed granular slopes as indicated by the close agreement between its predictions and the measurements. In the former test case, the proposed formulation successfully reproduces the variation of the normal stress on the rheometer top plate with shear rate, i.e. a transition in the state of the normal stress between being constant, dipping, and increasing quadratically as the shear rate increases. It maps the variation of the normal stress smoothly between the quasi-static and the inertia regimes. As to the latter test case concerning granular slope failure, the present formulation gives a good prediction of the incipient angle, i.e. the angle of the slope where grains on the surface starts to move, of both dry and immersed granular slopes including its dramatic increases with the initial packing fraction due to the frictional dilation/contraction. In the latter case, the proposed formulation performs much better than the classical saw model of dilation/contraction, especially when the granular bed dilates.

Following these analytical validations, the proposed dilation/contraction formulation is then integrated into a two-fluid continuum model for submerged granular flows which is

applied to simulate the full collapse process of underwater granular columns. Both collapsing column profiles and the excess fluid pressure simulated by the proposed model generally agree well with the measured data. Distinct collapsing behaviours of initially loosely- and densely-packed columns in the profile and interstitial fluid pressure due to the frictional dilation/contraction are well reproduced. The model without the frictional dilation/contraction effect clearly fails to capture the significant influence of initial packing fraction on the collapse. Integrating the proposed frictional dilation/contraction formulation helps us capture the column collapse from the initially static state to the final deposition.

Acknowledgments

This work is jointly supported by the Science and Technology Development Fund, Macau SAR (File no. SKL-IOTSC-2021-2023), a UK EPSRC grant (EP/R02491X/1), Open Research Fund Program of State Key Laboratory of Hydroscience and Engineering (sklhse-2019-B-01), Start-up Research Grant of University of Macau (File no. SRG2020-00023-IOTSC).

Funding

Supported by the Science and Technology Development Fund, Macau SAR (File no. SKL-IOTSC-2021-2023), a UK EPSRC grant (EP/R02491X/1), Open Research Fund Program of State Key Laboratory of Hydroscience and Engineering (sklhse-2019-B-01), Start-up Research Grant of University of Macau (File no. SRG2020-00023-IOTSC).

Declaration of Interests

The authors report no conflict of interest.

Author ORCID

H. Shi, https://orcid.org/0000-0002-0567-7948

Appendix A

A preliminary analysis on the magnitude of the shear strain γ_* is presented here.

Combining (3.5), (3.10) and (3.11), the non-dimensional change of frictional solid pressure due to the rearrangement of contact force chains under shear strain γ_* can be expressed as

$$\frac{\Delta p_s^e}{p_{s0}^e} = \exp\left[K\chi \frac{\phi_s\left(\phi_s - \phi_c\right)}{\phi_s - \phi_*}\gamma_* \right] - 1, \tag{A 1}$$

when $\phi_s > \phi_*$. Generally, the material parameter for dilatancy K has a value in the range of $1.0 \sim 25.0$ and an order of $O(10)$ (see Pailha & Pouliquen 2009; Bonnet, Richard & Philippe 2010; Gravish & Goldman 2014). The magnitude of χ is between 1.50 and 5.50 (see Hsu, Jenkins & Liu 2004; Lee & Huang 2018). The random loose-packing volume fraction of granular materials $\phi_* = 0.50 \sim 0.59$ and the random close-packing fraction $\phi^* = 0.61 \sim 0.64$ (van Wachem *et al.* 2001). The critical volume fraction of dilatancy ϕ_c has a value in the range of $\phi_* \sim \phi^*$. It is reasonable to expect that the non-dimensional increase of solid pressure in frictional dilation has an order of $O(1)$ and is limited by $\Delta p_s^e / p_{s0}^e < 10$. Therefore, according to (A 1), γ_* should be of the order of $O\left(10^{-2}\right) \sim O\left(10^{-1}\right)$.

Specifically, given $K = 13$, $\chi = 3.5$, $\phi_* = 0.55$, and $\phi_c = 0.58$, the variations of $\Delta p_s^e / p_{s0}^e$ with the shear strain γ_* in the cases of $\phi_s = 0.56$ for frictional contraction and $\phi_s = 0.60$ for frictional dilation are shown in figure A1. It illustrates that a small shear strain may lead to significant effects of frictional dilation/contraction, which is consistent with the assumption in section 3 that the changes in the frictional solid pressure due to rearrangement of contact force chains occur in a very short duration and the process can be regarded as transient in a continuum description.

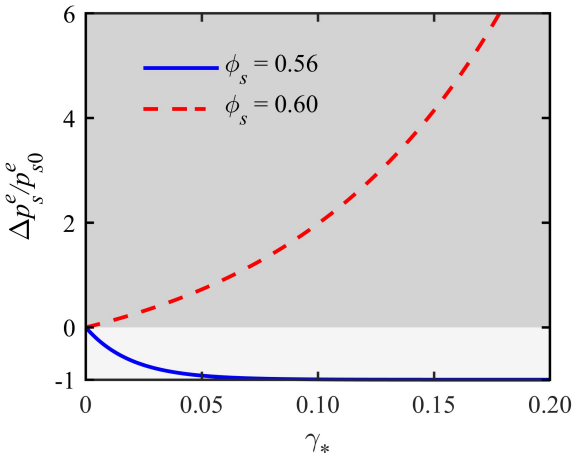

Figure A1. Variations of changes in frictional solid pressure p_s^e versus the shear strain γ_*. The dark grey area indicates the cases of dilation and the rest contraction.

The shear strain γ_* increases with the dimensionless shear rate I_d, which is defined as $I_d \equiv 2d_s \|\boldsymbol{S}_s\| / \sqrt{p_{s0}^e / \rho_s}$ in (3.13) and can also represent a shear strain being the product of the temporal period of microscopic rearrangement of contact force chain and the rate of macroscopic deformation. However, γ_* and I_d are not the same. As shown in Lu, Brodsky & Kavehpour (2007) and Chialvo, Sun & Sundaresan (2012), in granular media where the inter-grain frictional contacts predominates, I_d has a value of $O\left(10^{-6}\right) \sim O\left(10^{-1}\right)$. The orders of γ_* and I_d are distinct, and generally γ_* has a larger order.

To relate the frictional solid pressure to the shear rate of granular flows, a simple power relation, i.e. (3.14), is proposed for γ_*, which is rewritten here as

$$\gamma_* = c_1 \left(I_d\right)^{c_2}. \tag{A 2}$$

As the order of γ_* is generally larger than that of I_d and $I_d < 1$, c_2 should be in the range of $0 < c_2 < 1$. The coefficient c_1 needs to be determined based on the order of $\left(I_d\right)^{c_2}$ and should be in the range of $0 \sim O(10)$.

Appendix B

A validation of the two-phase SPH model in bed-load transport by laminar Poiseuille flow against the analytical solution of Ouriemi, Aussillous & Guazzelli (2009) is conducted.

In bed-load transport by laminar shear flow, the solid particles stay in continuous or

intermittent contact with neighboring grains in the bed (Aussillous *et al.* 2013) and the frictional inter-grain stresses predominate in the motion of the particles. Ouriemi, Aussillous & Guazzelli (2009) applied a continuum model to describe the bed-load transport in laminar viscous regime and for undisturbed Poiseuille flow they obtained an analytical solution of the flow field. It was found that the two-phase flow could be separated into four regions vertically regarding to the profiles of flow velocity. Region I corresponded to the pure fluid above the bed ($h_p \le z \le H$ with h_p being the bed height and H the full height of the two-phase flow), in which the profile of fluid velocity approached to that of the Poiseuille flow. Region IV was the immobile bed layer ($0 \le z \le h_c$ with h_c for the height of the static layer), where the velocities of both solid and fluid phase were zero. Regions II and III were mobile bed layers in which the slip between the two phases was little and neglected in the analytical solution. Region III ($h_c \le z \le h_p - d_s$) had a parabolic distribution of flow velocity and a negligible variation of porosity along the vertical direction. Region II ($h_p - d_s \le z \le h_p$) was a transition layer between region I and region III.

The present two-phase SPH model is applied to simulate the flow velocity profiles in the experiments of laminar bed-load transport conducted by Ouriemi, Aussillous & Guazzelli (2009). The fluid has a density of $\rho_f = 1.038\,\mathrm{g/cm^3}$ and a viscosity of $\nu_f = 3.56\times10^{-5}\,\mathrm{m^2/s}$. Two kinds of solid particles are used, i.e. glass grains with $\rho_s = 2.490\,\mathrm{g/cm^3}$ and $d_s = 132\,\mu\mathrm{m}$ and light PMMA grains with $\rho_s = 1.177\,\mathrm{g/cm^3}$ and $d_s = 193\,\mu\mathrm{m}$. The full height of the two-phase flow is $H = 30\,\mathrm{mm}$ and the bed height is $h_p = 15\,\mathrm{mm}$. For simplicity of numerical implementations, rather than keeping a constant flow rate as done in the experiments, we impose a pressure on the flow with a fixed gradient of $-\left(\partial p_f/\partial x\right)/\rho_f = 0.05\,\mathrm{m/s^2}$ and solve the steady velocity profile under the pressure. Accordingly, periodic boundary condition is applied in the longitudinal direction. The imposed pressure gradient leads to a Shields number of about $\theta = 0.21$ for the case with glass particles and $\theta = 1.45$ for the case with light PMMA particles. As the flow is in the viscous laminar regime, the stresses of the two phases due to fluid turbulence, i.e. $\boldsymbol{\sigma}_s^t$ in (5.10) and $\boldsymbol{\tau}_f^t$ in (5.12), vanish and hence the Smagorinsky coefficients in (5.13) are set to be zero. According to the experimental configurations in Ouriemi, Aussillous & Guazzelli

(2009), a random close-packing volume fraction of $\phi^* = 0.610$ and a random loose-packing volume fraction of $\phi_* = 0.550$ are set for both cases. The compressibility coefficient of glass grains is $G = 10^9$ Pa while that for PMMA particles is $G = 10^8$ Pa. Values of the coefficient χ are carefully determined so that the initial inter-grain pressure in the bed has a vertically linear profile, satisfying the static condition, and the porosity of the bed has a minor variation from the mean amount. In the simulations, $\chi = 4.85$ is set for the glass grains and $\chi = 4.87$ for the light PMMA particles. Initially, the mean porosities of the bed in both cases are 0.415. The other model parameters have the same values in both cases. The frictional dilation/contraction effect on inter-grain stresses is excluded in this problem as there is no experimental evidence for it, and it was also not considered in the analytical solution. Hence, in (5.5) $c_1 K = 0$ and $c_2 = 1.0$ are set. The friction coefficients $\mu_1 = 0.43$ and $\mu_2 = 0.82$ as well as $\sqrt{I_0} = 0.01$ are adopted as suggested in Ouriemi, Aussillous & Guazzelli (2009). A jamming fraction of $\phi_0 = 0.610$ is selected in the range of $\phi_* \sim \phi^*$. The coefficients $c_3 = 1.00$ and $c_4 = 0.10$ are determined following a sensitivity study of the velocity profiles. It is shown in the sensitivity study that altering the values of ϕ_0, c_3, or c_4 leads to a negligible change in the velocity profiles, especially in the case of glass beads. This conclusion is consistent with the fact that the frictional inter-grain stresses predominate in the bed-load transport by laminar shearing flows while the collisional solid stresses play a minor role. In the simulations, the entire two-phase flow is represented by a set of SPH particles having an initial size of $\Delta_p = 1\text{mm}$.

The computed steady profiles of fluid and solid velocities in the Poiseuille flow are compared with analytical results in figure B1. Following Ouriemi, Aussillous & Guazzelli (2009), we scale the length by the full height of the flow, i.e. $\bar{z} = z/H$, $\bar{h}_p = h_p/H$, and $\bar{h}_c = h_c/H$, and the velocity by $\left(\rho_s - \rho_f\right) g H^2 / \rho_f \nu_f$, i.e. $\bar{u} = u \rho_f \nu_f / \left(\rho_s - \rho_f\right) g H^2$. The numerical velocity profiles are in generally good agreement with the analytical results in the two cases with distinct Shields numbers. The present two-phase SPH model, specifically the integrated frictional constitutive law, performs reasonably in describing the contact-dominated bed-load transport by laminar shearing flows. The major difference between the numerical and the analytical results lies in the thickness of the mobile bed layer, which is partly

contributed by the numerical diffusion near the bed surface of a SPH method. In the case of glass particles with a small Shields number, the analytical thickness of mobile bed layer $\overline{h}_p - \overline{h}_c$ is about one particle diameter while the numerical value from the present model is more than two times the grain size. In the flow only one layer of particles on the bed surface moves and the assumption of a continuum description of the solid phase in the present model does not hold for this condition, which is the reason for the error in the numerical results. In the case of PMMA particles with a large Shields number, the present two-phase model performs much better. The analytical thickness of the mobile bed layer $\overline{h}_p - \overline{h}_c$ is more than seven times the particle diameter and the computed value by the present model is very close to the analytical solution. The velocity profiles in regions I, III, and IV are well reproduced (region II is too thin to be visible in the figures). It is shown in more cases with different Shields numbers that, when the thickness of mobile bed is greater than four particle layers in which the assumption of a continuum modelling of the solid phase holds, the present two-phase SPH model is applicable to bed-load transport by laminar shearing flows.

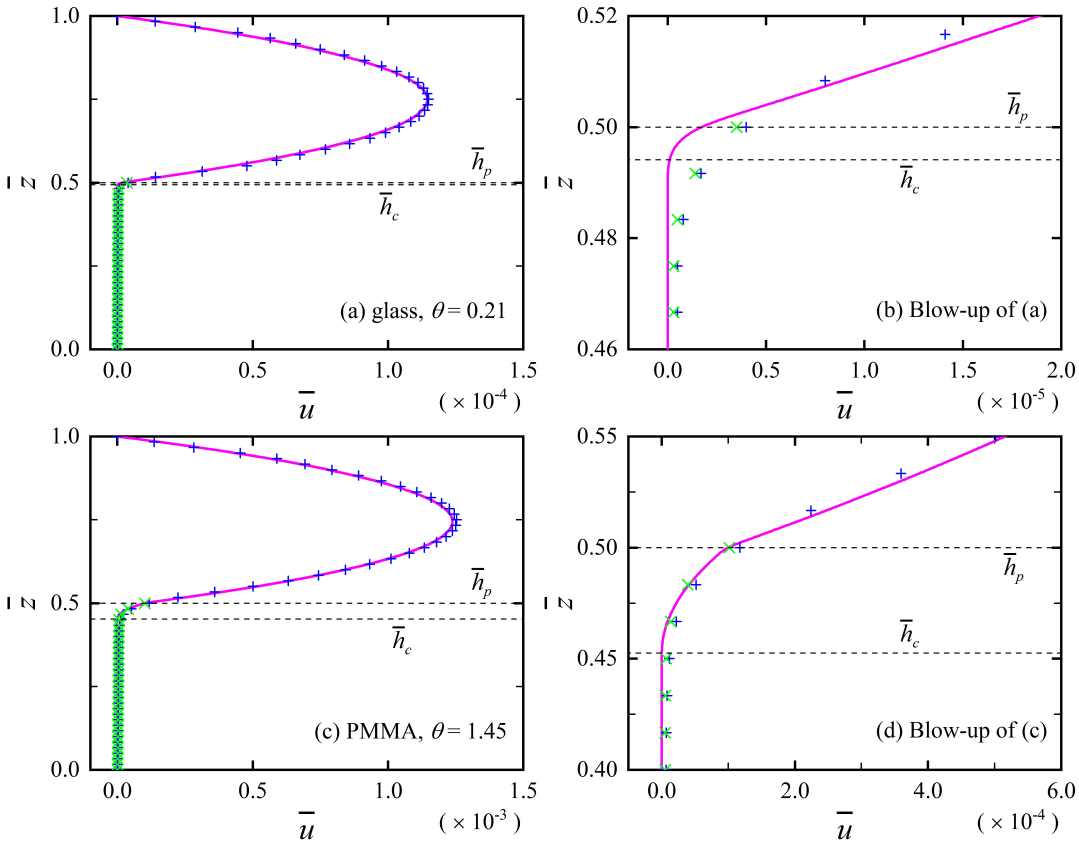

Figure B1. Comparisons of the numerical velocity profiles for the fluid (blue +) and the solid (green ×) phases by the present two-phase SPH model with the analytical solutions (magenta —) of Ouriemi, Aussillous & Guazzelli (2009). The dimensionless analytical results of the bed height $\overline{h}_p = h_p / H$ and the static bed layer height $\overline{h}_c = h_c / H$ are outlined in the figures by dashed lines. (a) and (b) are for the case of glass particles in which the Shields number is about $\theta = 0.21$ while (c) and (d) are for the case of light PMMA grains where $\theta = 1.45$.

Appendix C

The sensitivities of the computed column profiles by the present model in the loose packing case of collapse to adjustable model parameters and the formulation of inter-phase drag force are studied. It is shown in figures 6 and 7 that in the early stage of motion the present model predicts a faster collapse than the experimental observations, especially in the loose packing case.

Table C1 shows the sensitivities of the computed front position and column height at t = 0.66 s in the early stage and t = 3.96 s in the final period of the collapse with respect to adjustable parameters, i.e. the non-material parameters in table 1. For material parameters, the same values as those in section 5 are set. It should be noted that the adjustable parameter χ in the formula of p_{s0}^{e} is not included in table C1. χ is determined based on the initial condition for inter-grain pressure in static granular columns and should be fixed for each specific experimental configuration. It shows that the computed column profile is most sensitive to c_1 and c_2 for the frictional dilation/contraction effect. It is also highly sensitive to c_3 for the collisional solid pressure and less but still clearly to μ_2 and I_0 for friction coefficient. c_4 has a negligible effect on the results, implying that in the concerned immersed granular columns the viscous effect of interstitial fluid predominates in inter-grain collisions. With respect to c_1 and c_2, the sensitivities of the column profile at t = 0.66 s are similar to those of the final deposition at t = 3.96 s. However, the sensitivities of the profile at t = 0.66 s to c_3, μ_2, and I_0 markedly differ from those of the final deposition. Specifically, with respect to the three parameters, the sensitivities of the column heights at t = 0.66 s and t = 3.96 s are comparable while the front position at t = 3.96 s is more sensitive than that at t = 0.66 s. This difference in the sensitivities of the column profiles at t = 0.66 s and t = 3.96 s to

954 the parameters, especially to c_3, makes it very hard to achieve a good agreement between
955 numerical and experimental results in both the early stage and the final period of the collapse.
956 In section 5, the present model is calibrated primarily against the final deposition and the error
957 in column profiles at the early stage of collapse is left unaddressed. An underestimation of the
958 collisional solid pressure and the corresponding inter-grain shear resistance is likely the
959 reason for the computed faster collapse in the early stage.

960 The sensitivity of the computed column profile to the formulation of inter-phase drag
961 force is briefly examined to determine whether the reason for the computed quicker collapse
962 in the early stage is an underestimation of the drag force. In the present model, the
963 well-verified drag force model A of Gidaspow (1994) is utilized, expressed as (5.14) – (5.16).
964 Here, we denote the coefficient β in (5.14) as β_A. Taking the pressure drop of two-phase
965 flows only in the liquid phase, Gidaspow (1994) also proposed a model B for the drag force,
966 in which the coefficient β was denoted as β_B and $\beta_B = \beta_A / \phi_f$. As in immersed granular
967 flows volumetric fraction of the liquid phase ϕ_f always complies with $0 < \phi_f \le 1$, β_B
968 cannot be smaller than β_A and hence model B gives a larger inter-phase drag force than
969 model A. The computed profiles in the loose packing case by the present model with β_A and
970 the model with β_B are compared in figure C1. At t = 0.22 s, specifically during 0 – 0.44 s
971 before the thin-layer surge front appears, results of the two models are almost the same. At t =
972 0.66 s when the surge front of the column spreads, the collapse computed by the model with
973 β_B is slightly quicker than that by the present model. The difference between the column
974 profiles increases with time and is notable at t = 3.96 s, especially in the front position of the
975 column. The result of a larger drag force leading to a farther front position is consistent with
976 the conclusions in Shi *et al.* (2019) and Si, Shi & Yu (2018) and can be interpreted in terms of
977 the fact that in the surge front of the initially-loosely packed column the drag force acts as a
978 driving force and pulls solid grain forward. It is clearly illustrated that increasing the
979 liquid-solid drag force in the present model cannot slow down the collapse in the early stage
980 but results in an even quicker propagation of the surge front.

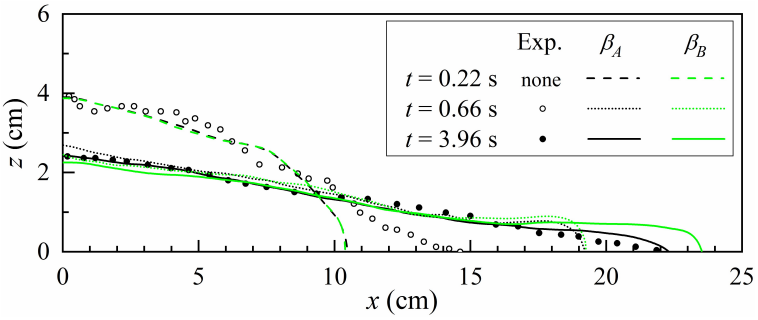

Figure C1. Sensitivities of computed column profiles in the loose packing case to the formulation of inter-phase drag force. β_A represents the present model using the model A of drag force in Gidaspow (1994), which is expressed as (5.14) – (5.16). β_B represents the two-phase model integrating the model B of Gidaspow (1994), in which $\beta_B = \beta_A / \phi_f$.

Parameters	Varying Values	t = 0.66 s in the Early Stage		t = 3.96 s in the Final Period	
		Front position (cm)	Column Height (cm)	Front position (cm)	Column Height (cm)
c_1	0, 2.5, 5.0, 7.5, 10.0	9.5, 18.9, 19.3, 19.2, 19.2	4.8, 2.6, 2.3, 2.1, 2.1	15.0, 22.2, 23.7, 22.7, 23.3	4.6, 2.5, 1.9, 1.8, 1.8
c_2	0.0, 0.1, 0.3, 0.6, 1.0	19.2, 18.9, 12.1, 9.8 , 9.6	2.1, 2.6, 4.8, 4.8, 4.8	23.1, 22.2, 15.2, 14.9, 14.1	1.8, 2.5, 4.5, 4.7, 4.7
c_3	0.75, 1.50, 2.0, 2.5, 3.0	21.8, 21.1, 19.9, 18.9, 17.8	2.0, 2.2, 2.4, 2.6, 2.8	30.0, 27.5, 24.4, 22.2, 20.2	1.8, 2.1, 2.3, 2.5, 2.6
c_4	0, 0.25, 0.50, 0.75, 1.00	18.8, 19.2, 18.6, 18.5, 18.4	2.6, 2.6, 2.6, 2.7, 2.6	22.2, 22.9, 21.3, 20.9, 21.2	2.4, 2.4, 2.5, 2.6, 2.5
μ_2	0.36, 0.60, 0.80, 1.00	21.1, 19.7, 18.9, 17.9	2.1, 2.3, 2.6, 2.7	27.6, 23.5, 22.2, 20.3	1.9, 2.3, 2.5, 2.6
I_0	0, 10^{-6}, 10^{-4}, 10^{-2}, 10^{0}	18.4, 18.6, 19.0, 20.3, 20.8	2.6, 2.6, 2.5, 2.2, 2.1	20.8, 21.5, 21.5, 25.1, 27.9	2.5, 2.5, 2.3, 2.0, 1.9

TABLE C1. Sensitivities of the computed front position and column height in the loose packing case by the present model with respect to adjustable parameters.

References

AUSSILLOUS, P., CHAUCHAT, J., PAILHA, M., MÉDALE, M. & GUAZZELLI, É. 2013 Investigation of the mobile granular layer in bedload transport by laminar shearing flows. *J. Fluid Mech.* **736**, 594-615.

BARKER, T., SCHAEFFER, D. G., BOHORQUEZ, P. & GRAY, J. M. N. T. 2015 Well-posed and ill-posed behaviour of the μ(I)-rheology for granular flow. *J. Fluid Mech.* **779**, 794-818.

BARKER, T., SCHAEFFER, D. G., SHEARER, M. & GRAY, J. M. N. T. 2017 Well-posed continuum equations for granular flow with compressibility and μ (I)-rheology. *Proc. R. Soc. A* **473**, 20160846.

995 BAUMGARTEN, A. S. & KAMRIN, K. 2019 A general fluid-sediment mixture model and constitutive
996 theory validated in many flow regimes. *J. Fluid Mech.* **861**, 721-764.
997 BONNET, F., RICHARD, T. & PHILIPPE, P. 2010 Sensitivity to solid volume fraction of gravitational
998 instability in a granular medium. *Granul. Matter* **12**, 317-325.
999 BOUCHUT, F., FERNÁNDEZ-NIETO, E. D., MANGENEY, A. & NARBONA-REINA, G. 2016 A two-phase
1000 two-layer model for fluidized granualr flows with dilatancy effects. *J. Fluid Mech.* **801**, 166-221.
1001 BOYER, F., GUAZZELLI, É. & POULIQUEN, O. 2011 Unifying suspension and granular rheology. *Phys.*
1002 *Rev. Lett.* **107**, 188301.
1003 CHAUCHAT, J. 2018 A comprehensive two-phase flow model for unidirectional sheet-flows. *J. Hydraul.*
1004 *Res.* **56** (1), 15-28.
1005 CHEN, X., LI, Y., NIU, X., CHEN, D. & YU, X. 2011 A two-phase approach to wave-induced sediment
1006 transport under sheet flow conditions. *Coastal Eng.* **58** (11), 1072-1088.
1007 CHIALVO, S., SUN, J. & SUNDARESAN, S. 2012 Bridging the rheology of granular flows in three
1008 regimes. *Phys. Rev. E* **85**, 021305.
1009 DALRYMPLE, R. A. & ROGERS, B. D. 2006 Numerical modeling of water waves with the SPH method.
1010 *Coast. Eng.* **53** (2-3), 141-147.
1011 DELANNAY, R., VALANCE, A., MANGENEY, A., ROCHE, O., RICHARD, P. 2017 Granular and
1012 particle-laden flows: from laboratory experiments to field observations. *J. Phys. D: Appl. Phys.*
1013 **50**, 053001.
1014 DREW, D. A. 1983 Mathematical modeling of two-phase flow. *Ann. Rev. Fluid Mech.* **15** (1), 261-291.
1015 DSOUZA, P. V. & NOTT, P. R. 2020 A non-local constitutive model for slow granular flow that
1016 incorporates dilatancy. *J. Fluid Mech.* **888**, R3.
1017 FORTERRE, Y. & POULIQUEN, O. 2008 Flows of dense granular media. *Annu. Rev. Fluid Mech.* **40**,
1018 1-24.
1019 GIDASPOW, D. 1994 *Multiphase Flow and Fluidization*, pp. 35-37. Academic.
1020 GONZALEZ-ONDINA, J. M., FRACCAROLLO, L. & LIU P. L. F. 2018 Two-level, two-phase model for
1021 intense, turbulent sediment transport. *J. Fluid Mech.* **839**, 198-238.
1022 GRAVISH, N. & GOLDMAN, D. I. 2014 Effect of volume fraction on granular avalanche dynamics.
1023 *Phys. Rev. E* **90**, 032202.
1024 GUO, X., PENG, C., WU, W. & WANG, Y. 2016 A hypoplastic constitutive model for debris materials.
1025 *Acta Geotech.* **11**, 1217-1229.
1026 HÉRAULT, A., BILOTTA, G. & DALRYMPLE, R. A. 2010 SPH on GPU with CUDA. *J. Hydraul. Res.*
1027 **48**(S1), 74-79.
1028 HEYMAN, J., DELANNAY, R., TABUTEAU, H. & VALANCE, A. 2017 Compressibility regularizes the
1029 μ(I)-rheology for dense granular flows. *J. Fluid Mech.* **830**, 553-568.
1030 HOUSSAIS, M. & JEROLMACK, D. J. 2017 Toward a unifying constitutive relation for sediment
1031 transport across environments. *Geomorphology* **277**, 251-264.
1032 HSU, T. J., JENKINS, J. T. & LIU, P. L. F. 2004 On two-phase sediment transport: sheet flow of massive

1033 particles. *P. Roy. Soc. A-Math. Phy.* **460** (2048), 2223-2250.
1034 IVERSON, R. M. & GEORGE, D. L. 2014 A depth-averaged debris-flow model that includes the effects
1035 of evolving dilatancy. I. Physical basis. *P. Roy. Soc. A-Math. Phy.* **470**, 20130819.
1036 JENKINS, J. T. & SAVAGE, S. B. 1983 A theory for the rapid flow of identical, smooth, nearly elastic,
1037 spherical particles. *J. Fluid Mech.* **130**, 187-202.
1038 JOHNSON, P. C. & JACKSON, R. 1987 Frictional-collisional constitutive relations for granular materials,
1039 with application to plane shearing. *J. Fluid Mech.* **176**, 67-93.
1040 JOHNSON, P. C., NOTT, P. & JACKSON, R. 1990 Frictional-collisional equations of motion for
1041 particulate flows and their application to chutes. *J. Fluid Mech.* **210**, 501-535.
1042 JOP, P., FORTERRE, Y. & POULIQUEN, O. 2006 A constitutive law for dense granular flows. *Nature* **441**,
1043 727-730.
1044 KAITNA, R., DIETRICH, W. E. & HSU, L. 2014 Surface slopes, velocity profiles and fluid pressure in
1045 coarse-grained debris flows saturated with water and mud. *J. Fluid Mech.* **741**, 377-403.
1046 LEE, C. H. & HUANG, Z. 2018 A two-phase flow model for submarine granular flows: With an
1047 application to collapse of deeply-submerged granular columns. *Adv. Water Resour.* **115**, 286-300.
1048 LU, K., BRODSKY, E. E. & KAVEHPOUR, H. P. 2007 Shear-weakening of the transitional regime for
1049 granular flow. *J. Fluid Mech.* **587**, 347-372.
1050 MAURIN, R., CHAUCHAT, J. & FREY, P. 2016 Dense granular flow rheology in turbulent bedload
1051 transport. *J. Fluid Mech.* **804**, 490-512.
1052 MERUANE, C., TAMBURRINO, A. & ROCHE, O. 2010 On the role of the ambient fluid on gravitational
1053 granular flow dynamics. *J. Fluid Mech.* **648**, 381-404.
1054 OURIEMI, M., AUSSILLOUS, P. & GUAZZELLI, É. 2009 Sediment dynamics. Part 1. Bed-load transport
1055 by laminar shearing flows. *J. Fluid Mech.* **636**, 295-319.
1056 PAILHA, M., NICOLAS, M. & POULIQUEN, O. 2008 Initiation of underwater granular avalanches:
1057 Influence of the initial volume fraction. *Phys. Fluids* **20**, 111701.
1058 PAILHA, M. & POULIQUEN, O. 2009 A two-phase flow description of the initiation of underwater
1059 granular avalanches. *J. Fluid Mech.* **633**, 115-135.
1060 REYNOLDS, O. 1885 On the dilatancy of media composed of rigid particles in contact. With
1061 experimental illustrations. *Lond. Edinb. Dubl. Phil. Mag.* **20** (127), 469-481.
1062 RONDON, L., POULIQUEN, O. & AUSSILLOUS, P. 2011 Granular collapse in a fluid: Role of the initial
1063 volume fraction. *Phys. Fluids* **23**, 073301.
1064 ROUX, S. & RADJAI, F. 1998 Texture-dependent rigid plastic behaviour. In *Proceedings: Physics of*
1065 *dry granular media* (ed. Herrmann H. J., Hovi J. P. & Luding S.), Sep. 1997, pp. 229-235.
1066 Springer.
1067 ROWE, P. W. 1962 The stress-dilatancy relation for static equilibrium of an assembly of particles in
1068 contact. *P. Roy. Soc. A-Math. Phy.* **269** (1339), 500-527.
1069 SHI, H., YU, X. & DALRYMPLE, R. A. 2017 Development of a two-phase SPH model for sediment
1070 laden flows. *Comput. Phys. Commun.* **221**, 259-272.

1071 SHI, H., SI, P., DONG, P. & YU, X. 2019 A two-phase SPH model for massive sediment motion in free
1072 surface flows. *Adv. Water Resour.* **129**, 80-98.
1073 SI, P., SHI, H. & YU, X. 2018 Development of a mathematical model for submarine granular flows.
1074 *Phys. Fluids* **30**, 083302.
1075 TRULSSON, M., ANDREOTTI, B. & CLAUDIN, P. 2012 Transition from the viscous to inertial regime in
1076 dense suspensions. *Phys. Rev. Lett.* **109** (11), 118305.
1077 VAN WACHEM, B. G. M., SCHOUTEN, J. C., VAN DEN BLEEK, C. M., KRISHNA, R. & SINCLAIR, J. L.
1078 2001 Comparative analysis of CFD models for dense gas-solid systems. *AIChE J.* **47** (5),
1079 1035-1051.
1080 WANG, C., WANG, Y., PENG, C. & MENG, X. 2017 Dilatancy and compaction effects on the submerged
1081 granular column collapse. *Phys. Fluids* **29**, 103307.
1082 WOOD, D. M. 1990 *Soil Behaviour and Critical State Soil Mechanics*. Cambridge University Press.